Whole-Brain Mapping of Choline Acetyltransferase Neurons Expression in Tree Shrew Compared with Mice

Yi-Lin Peng[1 #], Shuai-Deng Wang[1 #], Yi Wang[1], Zhi-Yi Zhang[1], Shan-Shan Zhang[1], Shuang-Shuang Liu[1], Zi-Ran Hong[1], Qi-Qi Xu[2], Yue-Xiong Yang[3], Fang-Liu[3], HuaWei Mu[4], Hao Wang[4], Yue-Ru Shen[2], Yu Wang[2], Xin-Ya Qin[2], Qing-Hong Shan[2], Peng Chen[2], Rong-Yu Liu[5], Jiang-Ning Zhou[2], Chen-Wei Wang[1, 2 *]

[1] Department of Anatomy, School of Basic Medicine, Anhui Medical University, Hefei 230032, Anhui, P. R. China.

[2] Institute of Brain Science, The First Affiliated Hospital of Anhui Medical University, Hefei 230022, Anhui, P. R. China.

[3] KIZ-SU Joint Laboratory of Animal Model and Drug Development, and Laboratory of Learning and Memory, Kunming Institute of Zoology, the Chinese Academy of Sciences, Kunming, Yunnan 650223, P. R. China

[4] MoE Key Laboratory of Brain-inspired Intelligent Perception and Cognition, Hefei National Research Center for Physical Sciences at the Microscale, Anhui Province Key Laboratory of Biomedical Imaging and Intelligent Processing, HFCNS Institute of Artificial Intelligence, National Engineering Laboratory for Brain-inspired Intelligence Technology and Application, University of Science and Technology of China, Hefei, 230026, P. R. China

[5] Anhui Geriatrics Institute, The First Affiliated Hospital of Anhui Medical University, Hefei, Anhui 230022, P. R. China

# Authors contributed equally to this work

* Corresponding author: Chen-Wei Wang: cwwang@ahmu.edu.cn, 86-551-65161047

ABSTRACT

The central cholinergic system regulates diverse neurological functions, learning, attention, arousal, sleep, emotion regulation and behavior control. As a close evolutionary relative of primates, tree shrew is a valuable comparative model for neurobiological investigation. However, the anatomical distribution of choline acetyltransferase-immunoreactive (ChAT-ir) neurons in its brain remains poorly characterized. Using ChAT immunofluorescence, we systematically mapped the whole-brain distribution and morphology of ChAT-ir neurons in tree shrew and compared them with mouse. In the neocortex, ChAT-ir neurons were absent in tree shrew, whereas mouse showed sparse cortical labeling. Semi-quantitative analyses of subcortical regions revealed the overall distribution was largely conserved, whereas tree shrew exhibited higher ChAT-ir neuronal density in the trochlear and prepositus nuclei compared to mice. ChAT-ir neurons were detected in the suprachiasmatic and supraoptic nuclei in the hypothalamus in tree shrew but not in mouse. Tree shrew ChAT-ir neurons showed greater dendritic complexity in caudate nucleus, medial septum, pedunculopontine/dorsal tegmental nuclei, and prepositus nucleus, while the horizontal limb of the diagonal band and oculomotor nuclei exhibited similar complexity across species. In the putamen, tree shrew has more complex distal dendrites but less complex proximal branches than mice. ChAT-ir neurons displayed a rostral-to-caudal density gradient in caudate, while mice showed largely uniform distributions of ChAT-, CB-, PV-, and CR-positive neurons across caudate putamen medial and lateral side. These findings provide a comprehensive mapping of ChAT-ir neurons in the tree shrew brain, highlighting significant interspecies differences and offering a structural framework for investigating cholinergic roles in diverse neural functions.

Keywords: Tree shrew; Choline acetyltransferase; Whole-brain mapping, Putamen; Caudate

INTRODUCTION

The tree shrew (Tupaia belangeri), owing to its close evolutionary proximity with primates, has emerged as an important alternative to non-human primates (NHPs) in biomedical research (Yao et al., 2024). It is increasingly employed to investigate fundamental biological and pathological processes, including sleep regulation (Coolen et al., 2012), viral infections (Feng et al., 2017; Ruan et al., 2013), myopia (Ku et al., 2022), and psychosocial stress-induced depression (Kozicz et al., 2008), with more recent work establishing models for neurodegenerative diseases. Notably, previous studies have validated the tree shrew as a suitable model for aging and Alzheimer's disease (AD) research, offering unique translational potential for studying neural mechanisms underlying cognitive decline (Guo et al., 2021; Li et al., 2023; Li et al., 2024; Pan et al., 2022; Wang et al., 2023).

Among the neural systems most relevant to cognitive and behavioral function, the brain's cholinergic network plays a central role in modulating neuronal excitability and synaptic transmission (Kaneko et al., 2000; Maurice et al., 2015). Through its widespread projections, cholinergic network supports sleep (Ni et al., 2016; Satchell et al., 2025), arousal (Fuller et al., 2011), sensory and motor processing as well as higher-order cognitive behaviors, including visuo-auditory perception (Maher et al., 2021), attention (Luchicchi et al., 2014; Sarter et al., 2016), motor (Xu et al., 2015), and cognition (Li et al., 2018). Of particular importance is cholinergic network in the dorsal striatum, which modulate corticostriatal plasticity (Deffains & Bergman, 2015) encode reward-related signals (Kljakic et al., 2022), and support behavioral flexibility (Okada et al., 2014), thereby contributing directly to cognitive processes. Central to this system is choline acetyltransferase (ChAT), a 69 kDa enzyme responsible for acetylcholine synthesis (Gill et al., 2003) and a widely used marker for identifying cholinergic neurons across species, from rodents to primates and humans (Araujo De Gois Morais et al., 2023; Chen et al., 2022; Nishijo et al., 2022; Shekari & Fahnestock, 2021; Williams et al., 2022a), in both developing and mature brains.

Although cholinergic systems have been extensively characterized in rodents and primates, knowledge of ChAT-ir neurons in the tree shrew (Tupaia) remains limited. To date, existing studies remain fragmented and are largely limited to localized immunohistochemical observations, rather than systematic, whole-brain analyses of ChAT-ir neuron distribution. Existing work has mainly focused on visual pathways, reporting dense cholinergic innervation of the lateral geniculate nucleus and visual cortex (Fitzpatrick et al., 1988), as well as distinct ChAT lamination patterns in the retina (Calvey et al., 2015; Knabe et al., 2007; Zhang et al., 2019). Notably, investigations of retinal cholinergic organization primarily pertain to peripheral sensory structures and do not constitute a comprehensive characterization of the central nervous system. In contrast, studies addressing the brain-wide distribution of cholinergic neuronal soma within the tree shrew central nervous system remain exceedingly scarce. At the phylogenetic level, genomic and comparative analyses place the tree shrew within Euarchonta and closer to primates than to rodents (Fan et al., 2018; Yao et al., 2024), highlighting its value as an intermediate model for evolutionary neurobiology. Despite increasing interest in the tree shrew as a translational species, a quantitative, brain-wide mapping of ChAT-ir neuronal soma has not yet been established, nor have direct and systematic comparisons with well-studied species such as the mouse been performed. Given the critical roles of acetylcholine in arousal (Fuller et al., 2011), attention(Luchicchi et al., 2014; Sarter et al., 2016), synaptic plasticity (Picciotto et al., 2012), and neuroendocrine regulation (Shi et al., 2008), a comprehensive delineation of the cholinergic architecture of the tree shrew brain is essential for defining its neurobiological and translational relevance. The present study addresses this gap by providing a comprehensive, brain-wide mapping of ChAT-ir neuronal distribution and morphology across the entire tree shrew brain and by directly contrasting these features with those observed in the mouse. This study aimed to investigate both conserved and species-specific organizational principles of the cholinergic system, offer new comparative insights in relation to primates, and establish a robust neuroanatomical framework for future functional, evolutionary, and disease-related investigations in this emerging model organism.

MATERIALS AND METHODS

Animals

Thirteen adult male tree shrews (8 months) were provided by the breeding colony in the Animal House Center of the Kunming Institute of Zoology, Kunming, P. R. China.

Three tree shrews were used for immunofluorescence, three for immunofluorescence-based three-dimensional reconstruction, three for immunohistochemistry, three for fluorescence in situ hybridization, and one for Western blot. Twelve C57BL/6J male mice (8- 10 weeks) were obtained from Shanghai Slac Laboratory Animal Co. Ltd. (Shanghai, China). Three mice were used for immunofluorescence, three for immunofluorescence-based three-dimensional reconstruction, three for immunohistochemistry, three for fluorescence in situ hybridization. Tree shrews and mice were housed individually in animal facilities under a 12-hour light/dark cycle (lights on at 8:00 AM) at 24-26℃ with *ad libitum* food and water conditions. All animal experiments were evaluated and approved by the Institutional Animal Care and Use Committee of Anhui Medical University (LLSC20211388). All efforts were made to minimize animal suffering as well as the number of animals used.

Tissue preparation

Animals were deeply anaesthetized with sodium pentobarbital (80 mg/kg, i.p.), perfused with phosphate-buffered saline (PBS, 0.1 M, pH 7.4) for 3 min and then with phosphate-buffered solution of 4% paraformaldehyde. After perfusion, the brains were removed and immersed in the same fixative at 4°C for three days (tree shrew) or one day (mouse). The brains were then immersed in 15% sucrose in PBS, followed by immersed in 30% sucrose in PBS until the tissue sank. The tissues were frozen and sectioned into 30 μm serial slices on a cryostat microtome (RWD Life Science, China).

The sections were stored at -20°C until use. Brains from one tree shrew and one mouse were sectioned into 100 μm serial slices on a vibrating microtome (B-S-1018, Bitelligen, China). The sections were stored at 4°C until use.

Immunofluorescent staining

The whole brain of the tree shrew was sectioned coronally at a thickness of 30 μm. For three-dimensional reconstruction, brain tissues were sectioned into 100 μm-thick slices. Brain sections were rinsed and permeabilized with 0.3% (v/v) Triton X-100 in PBS (PBST) for 1 h, blocked with 5% normal goat serum for 30 min, and incubated overnight at 4 °C with goat anti-ChAT primary antibody (1:100, AB144P, Millipore); rabbit anti-GABA primary antibody (1:500, A2052, Sigma-Aldrich) and mouse anti-tyrosine hydroxylase primary antibody (1:100, MAB5280, Millipore). After PBS rinsing, sections were incubated for 1 h at 37 °C with Donkey anti-Goat IgG (H+L) (1:200, 705-585-147, Jackson); Donkey anti-Rabbit IgG (H+L) (1:200, 711-545-152, Jackson) and Donkey anti-Mouse IgG (H+L) (1:200, 715-545-150, Jackson). Sections were washed again and counterstained with DAPI (1:2000). To assess antibody specificity, either the primary or secondary antibody was omitted in control experiments. Images were acquired using a Spin SR microscopy (Olympus, Japan).

Immunohistochemistry

Thirty-micrometer sections were treated in 0.5% PBST for 1 h. Antigen retrieval was carried out in citrate buffer for 20 min, followed by blocking with 5% normal donkey serum (017-000-121, Jackson ImmunoResearch, USA) in 0.5% PBST at 37 °C for 1 h. Sections were incubated with mouse monoclonal anti-Parvalbumin (PV) (MAB1572, Millipore, 1:1000, USA), anti-Calretinin (CR) (MAB1568, Millipore, 1:1000, USA) or anti-Calbindin (CB) (C9868, Sigma, 1:1000, USA) respectively for 1 h at 37℃ and overnight at 4℃, followed by biotinylated horse anti-mouse IgG (BA-2000, Vector Laboratories, 1:200, USA) and avidin-biotin peroxidase complex (PK-4000, Vector Laboratories, 1:200, USA). Sections were developed with 0.05% 3,3′-diaminobenzidine (Sigma-Aldrich, USA) and 0.25% NiSO4·6H2O (Sigma-Aldrich, USA) as chromogen. Sections were then dehydrated through graded ethanol, cleared in xylene, and cover slipped with mounting medium.

Three-dimensional reconstruction

To evaluate ChAT-ir neuronal morphology, 100-µm sections stained for ChAT and DAPI were imaged using a Spin SR microscope with a 30×objective to acquire stereoscopic views of the target brain regions. Images were acquired at a resolution of 2304×2304 pixels, with z-stacks collected at 1.0-µm intervals. All images were captured from the nucleus center to minimize overlap with adjacent regions. Imaging parameters (laser intensity, exposure time, threshold) were kept constant across all acquisitions. Imaris 9.3 software (Bitplane, Switzerland) was employed to quantify process length, soma area and soma volume, and to perform sholl analysis. Only ChAT-ir neurons with complete process length were included in process reconstruction. Custom settings for process reconstruction were: starting points = 10 μm, seed points = 2 μm, smooth= 2, sphere diameter =10 μm. The center of the soma was defined as the origin for each reconstructed cell. A series of concentric spheres was then generated at fixed radial intervals extending outward from the soma center. The number of intersections between cellular processes and each concentric sphere was automatically calculated at increasing radii. Each reconstructed cell was treated as an independent statistical unit. Intersection profiles were obtained for individual cells and averaged within each experimental group for subsequent analysis. Sholl intersection data were analyzed using two-way analysis of variance (ANOVA), with experimental group and radial distance as factors, followed by appropriate post hoc comparisons where applicable. This approach allowed for quantitative assessment of changes in process complexity as a function of distance from the soma.

Western blot analysis

To exam the sensitivity and specificity of antibody, western blot was performed following established procedures (Wang et al., 2025). Brain proteins were extracted by homogenizing tissue in ice-cold RIPA buffer containing 50 mM Tris–HCl (pH 7.6), 1% Triton X-100, 150 mM NaCl, 0.1% SDS, a protease inhibitor cocktail, and 0.5% sodium deoxycholate. The homogenate was centrifuged at 12,000 × g for 15 min at 4 °C, and protein concentration was determined by BCA assay. Proteins were resolved by 12% SDS-PAGE and transferred to membranes for western blotting. ChAT was detected using goat anti-ChAT (1:1000, AB144P, Millipore, USA) and HRP-conjugated anti goat IgG (1:2000, 330622, ADL, USA). Signals were detected using enhanced chemiluminescence (BL520B, Biosharp, Canada) on a chemiluminescence imaging system (Tanon-4600, China).

Fluorescence in situ hybridization and Imaging

Animals were deeply anesthetized with 1% (w/v) sodium pentobarbital. Cardiac perfusion was performed sequentially with 50 mL of 37◦C 1× PBS (phosphate buffered saline; dissolved in RNase-free water), 50 mL of ice-cold 1× PBS, and 50 mL of ice-cold 1% hydrogel monomer solution (HMS; 1% acrylamide, 0.0125% bis-acrylamide, 0.25% VA-044 initiator [w/v], 4% PFA in 1× PBS, RNase-free). Brains were dissected and incubated in 50 mL 4% HMS at 4◦C overnight. The embedding solution (25 ml of 4% HMS and 25 ml of 4% BSA) was degassed under vacuum for 10 min. Brains were then immersed in the solution and sealed for polymerization at 37◦C for 4 h. Embedded brains were trimmed and sectioned into 300 μm slices using a vibratome. Slices were cleared overnight at 37◦C in 4% SDS/0.2 M boric acid buffer (pH = 8.5) with gentle shaking, then washed three times in 0.3% PBST (1× PBS with 0.3% Triton X-100) at 37◦C for 1 h each, followed by a final wash in 1× PBS at room temperature. The hybridization protocol was adapted from the HCR 3.0 method (Choi et al., 2018; Zheng et al., 2025). Mouse brain slices were transferred to 50 mL tubes and incubated in 10 mL of 30% pre-hybridization buffer (30% formamide in 5× SSC) at 37◦C for 30 min with gentle shaking. Slices were then incubated overnight at 37◦C in 10 mL of probe hybridization buffer (30% formamide in 5× SSC containing a probe mixture; 400 nM per probe) with gentle shaking. The following day, slices were washed at 37◦C with 30% prehybridization buffer four times (2 × 15 min, then 2 × 30 min) with gentle shaking, followed by two washes at room temperature in 5× SSCTw (5× SSC with 0.1% Tween-20) for 15 min each. Samples were then equilibrated in pre-amplification buffer (5 × SSCTw) at room temperature for 30 min. Fluorescent hairpins were prepared by snap-cooling 200 µL of 3 µM hairpin stock in hairpin buffer (heated at 95◦C for 90 s, then cooled in the dark at room temperature for 30 min). The snap-cooled hairpins were added to 10 mL of amplification buffer. Samples were incubated overnight (>16 h) at room temperature in the dark with 1 mL of amplification buffer. Excess hairpins were removed by washing at room temperature in 5× SSCTw (2 × 5 min, 2 × 30 min), 0.5 × SSCTw (2 × 30 min), and 0.5× SSC (3 × 10 min) with gentle shaking. Prior to imaging, brain slices were incubated overnight in a refractive index (RI) matching medium composed of iohexol (650 g), urea (350 g), triethanolamine (140 g), and 210 mL of RNasefree water. The imaging chamber was filled with the same medium to ensure consistent optical properties during acquisition. Imaging was conducted using the VISoR platform (Wang et al., 2019).

ChAT-ir neurons density quantification in tree shrews and mice

The densities of ChAT‑ir neurons were quantified in 34 brain regions from three tree shrews and three mice. All sections were processed for immunofluorescence staining. Coronal sections were obtained at 0.18 mm intervals in tree shrews and 0.09 mm intervals in mice. For each section, two identical counting grids were placed bilaterally over the target region, and ChAT‑ir neurons within each grid were counted using ImageJ software. Regional density in each section was defined as the mean count from the two grids, and only cells co‑labeled with DAPI were included in the analysis. For each animal, regional density was calculated as the ChAT$^+$ cells numbers / total cells numbers. The total number of cells in each region was determined by DAPI-based nuclear counting. Bregma coordinates were assigned according to the tree shrew brain atlas (Jiang-Ning Zhou & Rong-Jun Ni, 2016) and the mouse stereotaxic atlas (Franklin & Paxinos, 2013).

Interneuron density quantification in tree shrews

The densities of interneurons were quantified in the caudate nucleus (Cd) and putamen (Pu) of tree shrews (n = 3) by normalizing the number of marker-positive interneurons to the total number of DAPI-labeled nuclei within the corresponding brain regions. Cd and Pu was subdivided into rostral (first third), middle (intermediate third), and caudal (last third) parts. Coronal sections were obtained at 0.30-mm intervals in tree shrews. In each section, the boundaries of Cd and Pu were manually delineated using white lines, and the number of DAPI-labeled nuclei was quantified using ImageJ software. Interneurons within the outlined regions were counted.

Statistical analysis

Cell body area and volume, along with process length, were analyzed using R version 4.21 (R Foundation for Statistical Computing, Vienna, Austria) with RStudio. Sholl analysis was preformed among multiple groups using two-way ANOVA, two-way repeated measures (RM) ANOVA, followed by Bonferroni *post hoc* tests in GraphPad Prism version 9.4.1 (GraphPad Software, San Diego, CA, USA). All datasets were checked for normality using the Kolmogorov-Smirnov test and for homogeneity of variance. Data are presented as mean±standard error of the mean (SEM). All statistical differences assessed by two-way ANOVA were considered significant at $P < 0.05$.

RESULTS

To assess antibody specificity, either the primary or secondary antibody was omitted in control experiments. No immunofluorescent signal was detected in negative control sections from tree shrew (Supplementary Figure S1A– C). Additionally, western blotting confirmed the effectiveness and specificity of the antibody in both tree shrew and mouse brains (Supplementary Figure S1D). These findings validate both the suitability and specificity of the antibody used in this study. The relative intensity of

ChAT-ir neurons was evaluated according to the criteria shown in Supplementary Figure S2. Nuclei without detectable ChAT‑ir were labeled as '-' (n=0), sparse distribution as '+' (1≤n≤10), moderate density as '++' (11≤n≤30), and high density as '+++' (n>30) within an individual field of view. For abbreviations of nuclei, refer to the Abbreviations List in Supplementary Table 1.

Overview of ChAT-ir neuron density and soma diameter in tree shrews and mice

The distribution of ChAT-ir neurons across brain regions in tree shrews and mice were summarized in Table 1, indicating their relative densities. Camera lucida drawings illustrated the distribution of ChAT-ir neurons in the tree shrew brain from rostral to caudal (Figure 1). Minimum and maximum densities for each nucleus in tree shrews and mice were presented as heatmaps (Figure 2A). In addition to density analysis based on maximum and minimum values for each brain area, six slices adjacent to the largest coronal section were further quantified for ChAT‑ir neuron counts, and soma diameters were also analyzed (Figure 2B). High densities of ChAT-ir neurons were observed in regions such as medial habenular nucleus (MHb), oculomotor nucleus, parvicellular part (3PC), Pre-Edinger-Westphal nucleus (PrEW), rostral linear nucleus of the raphe (RLi), trochlear nucleus (4N), caudal linear nucleus of the raphe (CLi), parabigeminal nucleus (PBG), oculomotor nucleus (3N), Dorsal tegmental nucleus (DTg), laterodorsal tegmental nucleus (LDTg), medial parabrachial nucleus (MPB), prepositus nucleus (Pr), vestibular nucleus (VES), while moderate densities were present in accumbens nucleus

(Acb), external globus pallidus (EGP), ventral pallidum (VP), islands of Calleja (ICj), sublenticular extended amygdala (EA), amygdalostriatal transition area (AST), medial septal nucleus (MS), septal and preoptic regions ventral part (LSv), nucleus of the vertical limb of the diagonal band (VDB), nucleus of the vertical limb of the diagonal band (HDB), Edinger-Westphal nucleus (EW), mesencephalic reticular formation (mRT), substantia nigra, reticular part (SNR), hypoglossal nucleus (12N), PTg (Pedunculopontine tegmental nucleus), subpeduncular tegmental nucleus (SPTg), ambiguus nucleus, compact part(Ambc), motor trigeminal nucleus (5N), abducens nucleus (6N), facial nucleus (7N), dorsal motor nucleus of vagus (10N), peritrigeminal zone (P5), superior olive (So) and solitary nucleus (Sol). The soma diameters in 4N, 5N and 12N were relatively larger than other nuclei, while those in MPB, RLi and EW were relatively smaller. Pairwise comparison heatmaps showing the statistical significance of the density (Figure 2C) and soma diameter (Figure 2D) of ChAT-ir neurons across different nuclei in the tree shrew.

Rhinencephalon

In the rhinencephalon, cell density ranges were in Layer 2 of the olfactory tubercle (Tu2), Layer 3 of the olfactory tubercle (Tu3), and the nucleus of the lateral olfactory tract (LOT) of tree shrews and mice, whereas no ChAT-ir signal was detected in the main olfactory bulb (MOB), accessory olfactory bulb (AOB), anterior olfactory nucleus (AON), or Layer 1 of the olfactory tubercle (Tu1) of tree shrews and mice (Table 1).

ChAT-ir fibers of tree shrews in the MOB exhibited a stratified distribution, with low density in the surface layers (outer nerve layer, ONL; glomerular layer, GL; external plexiform layer, EPI) and high density in the inner layers (mitral cell layer, MCL; internal plexiform layer, IPI; granule cell layer, GCL) (Figures 3A– F). Notably, ChAT-ir fibers of tree shrews in the EPI and GCL were aligned vertically toward the cortical surface. Soma staining of ChAT-ir neurons of tree shrews was observed in Tu2, Tu3 and LOT (Figures 3G– K). Notably, dense ChAT-ir fibers of tree shrews were present in LOT (Figures 3L).

Telencephalon

In the basal ganglia, Acb, EGP, VP, ICj, globus pallidus (GP), basal nucleus (Meynert, BN), and dorsal striatum of tree shrews and mice exhibited varying densities, whereas no ChAT-ir signal was detected in internal globus pallidus (IGP) or substantia nigra (SN) of tree shrews and mice (Table 1). No ChAT-ir soma was detected in the neocortex of tree shrews (Figures 4A, A1); however, ChAT-ir soma were detected in layer 2-4 of mouse cortex (Supplementary Figures 12A, A1). Soma staining of ChAT-ir neurons were found in the Cd, Pu, GP, VP (Figures 4B– F) and ic, ICj (Figures 4G, 4H) of tree shrews, and in CPu lateral side (CPu-L), CPu medial side (CPu-M), GP and VP (Supplementary Figures 12B– F) of mice brain. Soma staining of ChAT-ir neurons in BN of tree shrews (Figures 4I, 4J) and mice (Figures 4G, H) were found, which correlate with the sparse density in tree shrews and moderate dense in mice (Table 1).

In the amygdala, the medial amygdaloid nucleus (MeA), basolateral amygdaloid nucleus (BLA), central amygdaloid nucleus (CeA), EA and Ast of tree shrews and mice exhibited varying ChAT-ir densities, whereas no signal was detected in periamygdaloid cortex (PA), lateral amygdaloid nucleus (LA), basomedial amygdaloid nucleus (BMA), accessory basal nucleus (AB) of tree shrews. No ChAT-ir signals were detected in PA and AB of mice, however a small number of ChAT-ir signals were detected in the LA and BMA regions of the mice (Table 1). Soma staining of ChAT-ir neurons in tree shrews were found in BMA, MeA, CeA, BLA (Figures 5A– E), Ast, EA (Supplementary Figures 13A– B); however, no ChAT-ir neuron was found in AB (Figures 5A).

In the septal and preoptic regions, MS, LSv, septofimbrial nucleus (SFi), triangular septal nucleus (TS), VDB and HDB of tree shrews exhibited varying ChAT-ir soma density, whereas no signal was detected in lateral septal nucleus (LS), dorsal part (LSd), intermediate part (LSi), septohippocampal nucleus (SHi) or bed nucleus of the stria terminalis, medial division, anterior part (STMA) of tree shrews (Table 1). Soma staining of ChAT neurons in tree shrews were observed in LSv, VDB, STMA, MS, HDB and SFi, (Figures 5F– L), Lsi, SHi, TS (Supplementary Figures 13C– E). Notably, ChAT-ir soma were detected in LSv (Figures 5G), while rara ChAT-ir cell body was observed in the other subdivisions of LS.

Diencephalon

Notably, MHb exhibited dense ChAT‑ir density in both tree shrew and mouse (Table 1). Soma staining of ChAT-ir neurons in tree shrews were found in SON, SCN, MHb. (Figures 5 M– O), lateral preoptic nucleus (LPO), medial preoptic nucleus (MPO), VMH, and DMH (Supplementary Figures 13F– I).

Mesencephalon and metencephalon

In the mesencephalon, 3PC, PrEW, EW, RLi, mRt, SNR, 4N, 12N, PTg, SPTg, CLi, periaqueductal gray (PAG), PBG and dorsal raphe nucleus (DR) of tree shrews and mice exhibited varying ChAT-ir soma densities, whereas no signal was detected in the remaining nuclei of tree shrews. No ChAT-ir signals were detected in other brain regions of the mouse, except for the substantia nigra, compact part (SNC) (Table1). Soma staining of ChAT neurons in tree shrews were observed in the PAG, 4N, PTG, SNR, PBG, Rli, EW, 3PC, 12N (Figures 6A– H), DR SPTg mlf, CLi (Supplementary Figures 14A– D).

In the metencephalon, AmbC, 3N, motor 5N, 6N, 7N, 10N, Ves, DTg, LDTg, MPB, P5, So, Sol and Pr of tree shrews and mice exhibited varying ChAT-ir soma densities, whereas no signal can be detected in the remaining nuclei of tree shrews. No ChAT-ir signals were detected in other brain regions of the mouse, except for the ambiguus nucleus (Amb) regions (Table 1). Soma staining of ChAT neurons in tree shrews were observed in the DTg, LDTg, 3N, 5N, 6N, 7N, 10N, MPB, Pr, P5, VPO, IRt, AmbC (Figures 6I– S), Ves, VPO, Sol, So (Supplementary Figures 14E– H). We also examined the LC in both tree shrews and mice. ChAT immunostaining consistently failed to detect ChAT-ir neuronal soma in the locus coeruleus (LC) of either species, revealing only ChAT-ir nerve fibers. (Supplementary Figure S11 A– D)

Morphology analyses

To examine interspecies morphological differences of ChAT-ir neurons, eight anatomically defined brain regions of interest were selected from tree shrews and mice. Sholl analysis revealed that, compared with mice, the Cd/CPu-M (Figures 7A, Supplementary Figure S3A), PTg (Figures 7E, Supplementary Figure S3E), DTg (Figures 7G, Supplementary Figure S3G) and Pr (Figures 7H, Supplementary Figure S3H) in tree shrews exhibited more distal branching, as indicated by an increased number of intersections at greater distances from soma. In contrast, the MS in tree shrews showed greater proximal branching, indicated by an increased number of intersections at shorter distances from soma (Figures 7C, Supplementary Figure S3C). Notably, in the Pu/CPu-L, compared with mice, ChAT-ir neurons in tree shrews exhibited more complex distal branching and less complex proximal branching, as indicated by an increased number of intersections at 33-38 μm and a decreased number at 78-116 μm from soma (Figures 7B, Supplementary Figure S3B). In the of HDB (Figures 7D, Supplementary Figure S3D) and 3PC (Figures 7F, Supplementary Figure S3F), no significant differences in branch intersections were observed between tree shrews and mice.

The morphological characteristics of different nuclei were also compared within each species. ChAT-ir neurons of tree shrews exhibited relatively more branches in the DTg compared to other nuclei (Figures 7I), however this branching advantage was not observed in mice (Figures 7J). Furthermore, ChAT‑ir neurons of both tree shrews and mice exhibited fewer branches in the 3PC compared with other nuclei (Figures 7I, J). Notably, the Cd and Pu showed relatively high branch intersections and similar trends in branch complexity (Figures 7I, J).

The volumes and areas of ChAT‑ir cell bodies in the corresponding brain regions of tree shrew were significantly greater than those in mice (Figures 7K, L). However, as compared with mice, process length in the Cd, Pu, PTg, DTg and Pr in tree shrews increased significantly (Cd, P = 0.0001; Pu, P = 0.0367; PTg, P = 0.0001; DTg, P = 0.0001; Pr, P = 0.0003), while those in the MS, HDB, and 3PC decreased significantly (MS, P = 0.0151; HDB, P = 0.003; 3PC, P = 0.0181) (Figures 7M).

Distribution pattern of ChAT-ir interneuron in dorsal striatum

The ic separated the dorsal striatum into the Cd and Pu in the tree shrew, a pattern also observed in primates (Ni et al., 2021; Rice et al., 2011), but absent in mice. To further investigate this difference, the distributions of major interneurons subtypes — ChAT, CB, PV and CR — in Cd/Pu of tree shrews and in CPu-M/CPu-L of mice was systematically examined. In tree shrews, ChAT‑ir neurons in the Cd showed an overall trend of peak densities rostrally with subsequent reduction caudally (Figures 8A– C, M). The density of PV-positive neurons in the Pu exhibited a marked increase at approximately bregma −1.0 mm (Figures 8G– I, O; Supplementary Figure S5 A– L). The distribution of CB- and CR-positive neurons in Cd and Pu remained largely consistent along the anterior–posterior axis (Figures 8D– F, N; Figures 8J– L, P1; Supplementary Figure S4 A– L; Supplementary Figure S6 A– L). In mice, the expression patterns of ChAT-, CB-, PV-, and CR-positive neurons were largely comparable between the CPu-M and CPu-L regions, indicating that the mouse striatum represents an evolutionarily integrated and homogeneous structure (Figures 8A1– L1, M1– P1; Supplementary Figure S7 A– L, Supplementary Figure S8 A– L, Supplementary Figure S9 A– L). To further characterize Vgat+ (Vesicular GABA Transporter) neuron distribution in the dorsal striatum, HCR 3.0 together with VISoR imaging were applied to examine Vgat neurons in the tree shrew brain (Figures 9A– U). The results indicated a relatively homogeneous distribution of Vgat neurons along the rostral–caudal axis in both Cd and Pu respectively (Figure 9V). GABAergic neurons play a critical role in regulating striatal physiological functions. ChAT-, CB-, PV-, and CR − positive neurons represent major GABAergic neurons populations within the striatum. Characterizing their distribution patterns is therefore essential for understanding how GABAergic neurons contribute to striatal function. Notably, using double immunofluorescence staining for ChAT in combination with CB, PV, or CR, we found that CB-, PV-, and CR-positive neurons showed little to no colocalization with ChAT-ir neurons, indicating that these markers largely label distinct GABAergic neurons populations. Using double immunofluorescence staining for ChAT in combination with GABA showed the majority of ChAT-ir neurons in the striatum express GABA (Supplementary Figure S10 A – I).

DISSCUSION

This study presents a comprehensive brain-wide mapping of ChAT-ir neurons in the tree shrew, detailing their anatomical architecture across all major neuroanatomical divisions. High densities of ChAT-ir neurons were observed in MHb, 3PC, PrEW, RLi, 4N, CLi, PBG, 3N, DTg, LDTg, MPB, Pr, VES, as well as in Acb, EGP, VP, ICj, EA, AST, MS, LSv, VDB, HDB, EW, mRT, SNR, 12N, PTg, SPTg, Ambc, 5N, 6N, 7N, 10N, P5, So and Sol with moderate densities. The global distribution of ChAT-ir neurons in the tree shrew was strikingly similar to that described in the mouse and other species (Williams et al., 2022a; Woolf et al., 1984), suggesting conserved principles of cholinergic organization across species. Beyond establishing this anatomical framework, the present work provides a systematic interspecies comparison of ChAT-ir neuron density and morphology across the telencephalon, diencephalon, mesencephalon, metencephalon, and myelencephalon, revealing both conserved and region-specific divergence between tree shrews and mice. Moreover, this research provides a comprehensive assessment of interneuron distributions in the dorsal striatum across both species.

Comparative neuroanatomical studies indicate that the cholinergic system follows a largely conserved organizational framework across mammals, while exhibiting pronounced species-specific specializations. In humans, a distinctive feature of this system is the presence of ChAT-ir neuronal soma within the cerebral cortex, most prominently in the parietal association cortex, where ChAT-ir neurons are primarily localized to layers II–III (Benagiano et al., 2003; Williams et al., 2022). In contrast, studies in NHPs—including great apes such as chimpanzees (Raghanti et al., 2008), gibbons (Williams et al., 2022), and macaques (Amaral & Bassett, 1989; Hedreen et al., 1983; Mesulam et al., 1984; Raghanti et al., 2008)—have consistently demonstrated a cholinergic nuclear organization that closely resembles that of humans at the subcortical level, encompassing basal forebrain and brainstem cholinergic nuclei, but without detectable cortical ChAT-ir neuronal soma when examined using comparable immunohistochemical approaches. Together, these observations support the prevailing view that cortical cholinergic neurons represent a derived feature that may be specific to the human lineage. In rodents, including murid species, ChAT-ir neuronal soma has been reported in the cerebral cortex (Kruger et al., 2012; Calvey et al., 2015). Consistent with these reports, we observed sparse ChAT labeling in cortical layers II–IV of mice in the present study. In contrast, no ChAT-ir neurons were detected in the neocortex of tree shrews. Instead, ChAT-ir neurons in the tree shrew were robustly distributed across basal forebrain and brainstem nuclei, while cortical ChAT-ir soma were absent. This organizational pattern closely parallels that reported in macaques and other NHPs rather than the rodent condition, suggesting that the tree shrew retains a primate-like ancestral cholinergic blueprint without exhibiting the derived cortical cholinergic phenotype characteristic of humans. Within this evolutionary framework, our findings position the tree shrew as a valuable intermediate model for comparative neuroanatomical studies. The cholinergic organization of the tree shrew appears more complex and regionally differentiated than that of rodents, yet it does not display the fully derived cortical cholinergic phenotype observed in humans. This intermediate pattern is consistent with phylogenomic evidence placing Tupaia within the Euarchonta clade and evolutionarily closer to primates than to rodents (Fan et al., 2018; Yao et al., 2024). Collectively, these results further support the hypothesis that cortical cholinergic neurons represent a human-specific evolutionary innovation, while the tree shrew preserves a primate-like ancestral organization of the cholinergic system. At present, comprehensive whole-brain mapping of ChAT-ir neurons in NHPs remain limited, underscoring the need for further systematic mapping efforts. In this context, our whole-brain analysis of the tree shrew provides an important evolutionary reference point for distinguishing conserved mammalian features from rodent-specific adaptations and human-derived specializations.

Cholinergic neurons in the basal nucleus are essential for cognitive function, and their dysfunction is associated with various neurological disorders, particularly dementias (Chen et al., 2023). Basal forebrain cholinergic projection neurons, particularly those in the nucleus basalis of Meynert, are among the earliest neuronal populations to exhibit tauopathy in AD (Lin et al., 2022). Multiple anatomical studies have shown that cholinergic neurons in the nucleus basalis of Meynert are key components of the basal forebrain and provide extensive cholinergic innervation to the cerebral cortex (Chen et al., 2016; Gratwicke et al., 2013). In our study, ChAT-ir neurons were observed at a sparse density in the nucleus basalis of Meynert in the tree shrew brain. Given their closer genetic affinity to primates than to rodents, tree shrews represent a valuable translational model for advancing research on cognitive function and AD, especially studies focusing on the cholinergic system.

We quantitatively compared the density of ChAT-ir neurons in the major nuclei expressing cholinergic markers between tree shrews and mice. The results showed that the overall densities of ChAT-ir neurons were largely consistent across most brain regions, indicating that the organizational principles of the cholinergic system are evolutionarily conserved among species. Previous studies have demonstrated that cholinergic neurons play a crucial role in modulating neuronal excitability and synaptic transmission (Picciotto et al., 2012), thereby supporting visuomotor integration (Fitzpatrick et al., 1988) as well as visceral and neuroendocrine regulation (Mason et al., 1983; Picciotto et al., 2012; Tago et al., 1987), which are essential for complex sensorimotor and homeostatic processes (Gorbatyuk et al., 2021). In this context, the enhanced cholinergic modulation observed in tree shrews may be related to their diurnal lifestyle and strong reliance on vision, necessitating greater cholinergic influence in brain regions associated with visuomotor coordination and neuroendocrine control.

Compared with mice, tree shrews exhibited higher densities of ChAT-ir neurons in related nuclei, such as 4N and Pr in our study. Previous studies have demonstrated that, as diurnal animals, tree shrews exhibit enhanced cholinergic modulation in hypothalamic regions involved in circadian rhythm regulation as well as osmoregulatory and neuroendocrine balance (Ni et al., 2021). Notably, ChAT-ir neurons were detected in several related nuclei of the tree shrew brain, including SCN and SON, where no such labeling was observed in mice.

Neuronal morphology is a well-established criterion for classifying neuron types and inferring network connectivity (Zeng & Sanes, 2017), its characterization thus provides critical insights into information processing and signal transmission within local circuits (Spruston, 2008). Prior studies have demonstrated size differences in ChAT-ir interneurons between the dorsal/ventral striatum (Brauer et al., 2000; Lehericy et al., 1989; Mesulam et al., 1984; Prensa et al., 2003) and Cd/Pu (Holt et al., 1996), with striatal ChAT-ir interneuron volume correlating inversely with density (Bernacer et al., 2007). In the present study, ChAT-ir neurons in the Cd, MS, PTg, DTg and Pr of tree shrews exhibit greater dendritic arbor complexity than their murine counterparts. Tree shrews also display larger soma volume and surface area compared to mice in the Cd, Pu, HDB, PTg, 3PC, DTg and Pr. These morphological specializations may reflect the roles of these nuclei as higher-order brain regions mediating complex functions including emotion, learning, memory, and sleep regulation. Conversely, HDB and 3PC cholinergic neurons show comparable dendritic complexity across species, consistent with their status as evolutionarily conserved nuclei regulating fundamental homeostatic functions. However, In the Pu, tree shrew cholinergic neurons exhibit increased distal dendritic branching but reduced proximal branching relative to mice. This species-specific dendritic patterning may suggest differential cholinergic signal integration: mice may prioritize proximal cholinergic input, whereas tree shrews may possess enhanced capacity for distal cholinergic signal detection.

In primates, the dorsal striatum is anatomically divided into Cd and Pu (Araujo De Gois Morais et al., 2023; Crittenden & Graybiel, 2011), each subregion linked to distinct cortical areas and functional domains. Functionally, Cd is implicated in motor responses (Kesner & Gilbert, 2006), motor skill learning (Choi et al., 2020), and psychiatric disorders (Vostrikov & Uranova, 2020), whereas the Pu contributes to motor learning (Liebrand et al., 2020), auditory processing (Salisbury et al., 2021), addiction (Ersche et al., 2021), and neuropsychiatric pathologies (Kolomeets & Uranova, 2020). Our findings revealed a distinct rostrocaudal distribution of ChAT-ir neurons in the Pu of tree shrews, suggesting specialized cholinergic regulation that may support fine motor control and sensory integration (Abudukeyoumu et al., 2019). Given the established role of striatal cholinergic interneurons in modulating corticostriatal transmission and ameliorating motor learning deficits in parkinsonism, the distinctive Pu organization in tree shrews highlights their potential as a valuable model for motor disorders research (Laverne et al., 2022).

Their activity in the dorsomedial striatum is particularly critical for reversal learning and decision-making, while dysfunction of these neurons has been implicated in cognitive impairments observed in neuropsychiatric disorders (Ni et al., 2021; Okada et al., 2014). Interneurons within the dorsal striatum provide critical inhibitory regulation, integrate cortical and thalamic inputs, influence local network oscillations, and support synaptic plasticity, thereby enabling fine motor coordination, adaptive behavior, and cognitive flexibility. Dysfunction of these interneurons has been linked to motor and cognitive disorders, underscoring their importance in normal and pathological basal ganglia function (Rice et al., 2011).

A recent study established a high-resolution map of PV-, CB-D28k-, and CR-positive neurons in cerebrum of the tree shrew brain, providing a reliable and systematic framework of cell-type distributions for tree shrew neuroanatomical research (Zhang et al., 2025). Here, we systematically examined the distribution of ChAT-ir neurons in whole brain, thereby providing a valuable supplement for tree shrew neuroanatomical research. The dorsal striatum functions as a central hub integrating motor and cognitive processes, relying on diverse interneuron populations to regulate neuronal communication and network dynamics (Calabresi et al., 2000; Smeets et al., 2000). ChAT-, PV-, CB-, and CR-immunoreactive neurons were found to be widely distributed throughout the dorsal striatum of both tree shrews and mice, suggesting a conserved organization framework of striatal interneurons across these species. In tree shrews, ChAT‑ir neurons in Cd exhibited peak densities in rostral regions that declined caudally, whereas those in Pu consistently remained at relatively low density. However, in tree shrews, PV neurons in Cd and Pu displayed a rostral‑to‑caudal decline in density, whereas in mice, PV neurons in both lateral and medial caudate–putamen showed the reverse gradient. This regional disparity may reflect distinct excitability and input properties of PV interneurons across subregions such as the dorsomedial and dorsolateral striatum (Lee et al., 2017; Nakano et al., 2018). In mice, ChAT‑ir neurons in both lateral and medial caudate–putamen displayed patterns similar to those in the tree shrew Cd. This finding suggests a Cd-like organization within the rodent striatum. Notably, the cytoarchitectonic organization of the tree shrew striatum more closely resembles that of primates, and its well-developed striatal circuitry may facilitate advanced motor capacities required for arboreal locomotion, including climbing, leaping, and jumping (Ni et al., 2021). Collectively, these findings underscore the critical role of striatal interneuron diversity in health and disease, and highlight the tree shrew as an informative model for comparative and translational studies of dorsal striatum organization and pathology.

Significance: This study provides the comprehensive, brain-wide mapping of ChAT-ir neurons in the tree shrew and reveals pronounced interspecies differences in their regional distribution and dendritic morphology compared with mice. These findings establish an anatomical framework for investigating the roles of cholinergic neurons in visual processing, circadian rhythm regulation, and cognitive–motor functions, as well as their potential involvement in neurodegenerative disorders. Importantly, by comparing the distribution density of distinct interneuron populations within the dorsal striatum across species, our results offer novel insights into the evolutionary organization and functional specialization of striatal interneurons.

Limitation: Several limitations of the present study should be acknowledged. First, our comparative analysis was limited to tree shrews and mice, and the absence of data from a broader range of species—particularly NHPs—restricts the generalizability of our evolutionary interpretations. Future studies incorporating wider phylogenetic sampling will be necessary to more fully delineate the evolutionary trajectories of striatal cholinergic interneurons. Second, although we identified both shared and species-specific features in the brain-wide distribution of ChAT neurons between tree shrews and mice, the functional implications of these similarities and differences for neural circuit operation and behavior remain unknown and warrant further investigation.

CONCLUSION

This study presents a brain-wide mapping of ChAT-immunoreactive neurons in the tree shrew, uncovering notable interspecies differences in their distribution and dendritic morphology compared with mice. These findings establish a neuroanatomical framework for exploring cholinergic contributions to offer valuable insights for disease research.

Author Contributions:

Conceptualization: Chen-Wei Wang; Data curation: Chen-Wei Wang, Yi-Lin Peng, Shuai-Deng Wang, Zhi-Yi Zhang, Shan-Shan Zhang, Shuang-Shuang Liu, Zi-Rang Hong, Qi-Qi Xu,; Funding acquisition: Chen-Wei Wang, Yu Wang, Xin-Ya Qin, Hua-Wei Mu, Hao Wang, Peng Chen; Project administration: Chen-Wei Wang, Jiang-Ning Zhou; Resources: Chen-Wei Wang, Yue-Xiong Yang, Hua-Wei Mu, Hao Wang, Yu Wang, Xin-Ya Qin, Qing-Hong Shan, Peng Chen, Rong-Yu Liu; Supervision: Chen-Wei Wang; Validation: Yi Wang, Yi-Lin Peng; Visualization: Yi-Lin Peng, Yue-Ru Shen, Zhi-Yi Zhang; Investigation: Yue-Xiong Yang and Hua-Wei Mu, Hao Wang; Writing–original draft: Chen-Wei Wang, Shuai-Deng Wang, Yi Wang, Yi-Lin Peng; Writing – review & editing: Chen-Wei Wang, Yi-Lin Peng, Yi Wang, Zhi-Yi Zhang.

Acknowledgement:

We would like to acknowledge J. Wang, Q. Wang, Q. Du and L. Guo for their assistance in data collection and analysis. We also would like to acknowledge the Multimodality Imaging Center and the Intelligent Computing Platform of the Institute of Artificial Intelligence of Hefei Comprehensive National Science Center for the imaging facilities and the computing resources.

Funding:

This work was supported by the STI2030-Major Projects (2022ZD0205202), the National Natural Science Foundation of China (32200798, 82201671), the Institute of Artificial Intelligence of Hefei Comprehensive National Science Center (23YGXT004, Y1022502), Anhui Provincial Natural Science Foundation (2408085Y043), the Anhui

Province University Scientific Research Project (KJ2021A0212), the Anhui Medical University Research Funding (2021xkj008).

Declarations

Conflict of Interest: The authors declare no conflict of interest.

Ethical Approval: Approval was obtained from the ethics committee of the Ethics Committee of Anhui Medical University (LLSC20211388).

Abudukeyoumu N, Hernandez-Flores T, Garcia-Munoz M, et al. 2019. Cholinergic modulation of striatal microcircuits. *Eur J Neurosci*, **49**(5): 604-622.

Amaral DG & Bassett JL. 1989. Cholinergic innervation of the monkey amygdala: an immunohistochemical analysis with antisera to choline acetyltransferase. *J Comp Neurol*, **281**(3): 337-361.

Araujo De Gois Morais PL, De Souza Cavalcante J, Engelberth RC, et al. 2023. Morphology and morphometry of interneuron subpopulations of the marmoset monkey (Callithrix jacchus) striatum. *Neurosci Res*, **192**: 37-47.

Benagiano V, Virgintino D, Flace P, et al. 2003. Choline acetyltransferase-containing neurons in the human parietal neocortex. *Eur J Histochem*, **47**(3): 253-256.

Bernacer J, Prensa L, Gimenez-Amaya JM. 2007. Cholinergic interneurons are differentially distributed in the human striatum. *PLoS One*, **2**(11): e1174.

Brauer K, Hausser M, Hartig W, et al. 2000. The core-shell dichotomy of nucleus accumbens in the rhesus monkey as revealed by double-immunofluorescence and morphology of cholinergic interneurons. *Brain Res*, **858**(1): 151-162.

Calabresi P, Centonze D, Gubellini P, et al. 2000. Synaptic transmission in the striatum: from plasticity to neurodegeneration. *Prog Neurobiol*, **61**(3): 231-265.

Calvey T, Patzke N, Kaswera-Kyamakya C, et al. 2015. Organization of cholinergic, catecholaminergic, serotonergic and orexinergic nuclei in three strepsirrhine primates: Galago demidoff, Perodicticus potto and Lemur catta. *J Chem Neuroanat*, **70**: 42-57.

Chen L, Yin D, Wang TX, et al. 2016. Basal Forebrain Cholinergic Neurons Primarily Contribute to Inhibition of Electroencephalogram Delta Activity, Rather Than Inducing Behavioral Wakefulness in Mice. *Neuropsychopharmacology*, **41**(8): 2133-2146.

Chen ZR, Huang JB, Yang SL, et al. 2022. Role of Cholinergic Signaling in Alzheimer's Disease. *Molecules*, **27**(6).

Chen ZY, Yang YL, Li M, et al. 2023. Whole-brain neural connectivity to cholinergic neurons in the nucleus basalis of Meynert. *J Neurochem*, **166**(2): 233-247.

Choi HMT, Schwarzkopf M, Fornace ME, et al. 2018. Third-generation in situ hybridization chain reaction: multiplexed, quantitative, sensitive, versatile, robust. *Development*, **145**(12).

Choi Y, Shin EY, Kim S. 2020. Spatiotemporal dissociation of fMRI activity in the caudate nucleus underlies human de novo motor skill learning. *Proc Natl Acad Sci U S A*, **117**(38): 23886-23897.

Coolen A, Hoffmann K, Barf RP, et al. 2012. Telemetric study of sleep architecture and sleep homeostasis in the day-active tree shrew Tupaia belangeri. *Sleep*, **35**(6): 879-888.

Crittenden JR & Graybiel AM. 2011. Basal Ganglia disorders associated with imbalances in the striatal striosome and matrix compartments. *Front Neuroanat*, **5**: 59.

Deffains M & Bergman H. 2015. Striatal cholinergic interneurons and cortico-striatal synaptic plasticity in health and disease. *Mov Disord*, **30**(8): 1014-1025.

Dimanico MM, Klaassen AL, Wang J, et al. 2021. Aspects of tree shrew consolidated sleep structure resemble human sleep. *Commun Biol*, **4**(1): 722.

Ersche KD, Lim TV, Murley AG, et al. 2021. Reduced Glutamate Turnover in the Putamen Is Linked With Automatic Habits in Human Cocaine Addiction. *Biol Psychiatry*, **89**(10): 970-979.

Fan Y, Luo R, Su LY, et al. 2018. Does the Genetic Feature of the Chinese Tree Shrew (Tupaia belangeri chinensis) Support Its Potential as a Viable Model for Alzheimer's Disease Research? *J Alzheimers Dis*, **61**(3): 1015-1028.

Feng Y, Feng YM, Lu C, et al. 2017. Tree shrew, a potential animal model for hepatitis C, supports the infection and replication of HCV in vitro and in vivo. *J Gen Virol*, **98**(8): 2069-2078.

Fitzpatrick D, Conley M, Luppino G, et al. 1988. Cholinergic projections from the midbrain reticular formation and the parabigeminal nucleus to the lateral geniculate nucleus in the tree shrew. *J Comp Neurol*, **272**(1): 43-67.

Franklin KBJ & Paxinos G. 2013. Paxinos and Franklin's The mouse brain in stereotaxic coordinates. Fourth edition. Amsterdam: Academic Press, an imprint of Elsevier.

Fuller PM, Sherman D, Pedersen NP, et al. 2011. Reassessment of the structural basis of the ascending arousal system. *J Comp Neurol*, **519**(5): 933-956.

Gill SK, Bhattacharya M, Ferguson SS, et al. 2003. Identification of a novel nuclear localization signal common to 69- and 82-kDa human choline acetyltransferase. *J Biol Chem*, **278**(22): 20217-20224.

Gratwicke J, Kahan J, Zrinzo L, et al. 2013. The nucleus basalis of Meynert: a new target for deep brain stimulation in dementia? *Neurosci Biobehav Rev*, **37**(10 Pt 2): 2676-2688.

Guo Y, Wang L, Lu J, et al. 2021. Ginsenoside Rg1 improves cognitive capability and affects the microbiota of large intestine of tree shrew model for Alzheimer's disease. *Mol Med Rep*, **23**(4).

Hedreen JC, Bacon SJ, Cork LC, et al. 1983. Immunocytochemical identification of cholinergic neurons in the monkey central nervous system using monoclonal antibodies against choline acetyltransferase. *Neurosci Lett*, **43**(2-3): 173-177.

Holt DJ, Hersh LB, Saper CB. 1996. Cholinergic innervation in the human striatum: a three-compartment model. *Neuroscience*, **74**(1): 67-87.

Kaneko S, Hikida T, Watanabe D, et al. 2000. Synaptic integration mediated by striatal cholinergic interneurons in basal ganglia function. *Science*, **289**(5479): 633-637.

Kesner RP & Gilbert PE. 2006. The role of the medial caudate nucleus, but not the hippocampus, in a matching-to sample task for a motor response. *Eur J Neurosci*, **23**(7): 1888-1894.

Kljakic O, Janickova H, Skirzewski M, et al. 2022. Functional dissociation of behavioral effects from acetylcholine and glutamate released from cholinergic striatal interneurons. *FASEB J*, **36**(2): e22135.

Koga T, Bellier JP, Kimura H, et al. 2013. Immunoreactivity for Choline Acetyltransferase of Peripheral-Type (pChAT) in the Trigeminal Ganglion Neurons of the Non-Human Primate Macaca fascicularis. *Acta Histochem Cytochem*, **46**(2): 59-64.

Kolomeets NS & Uranova NA. 2020. Numerical density of oligodendrocytes and oligodendrocyte clusters in the anterior putamen in major psychiatric disorders. *Eur Arch Psychiatry Clin Neurosci*, **270**(7): 841-850.

Kozicz T, Bordewin LA, Czeh B, et al. 2008. Chronic psychosocial stress affects corticotropin-releasing factor in the paraventricular nucleus and central extended amygdala as well as urocortin 1 in the non-preganglionic Edinger-Westphal nucleus of the tree shrew. *Psychoneuroendocrinology*, **33**(6): 741-754.

Kruger JL, Patzke N, Fuxe K, et al. 2012. Nuclear organization of cholinergic, putative catecholaminergic, serotonergic and orexinergic systems in the brain of the African pygmy mouse (Mus minutoides): organizational complexity is preserved in small brains. *J Chem Neuroanat*, **44**(1): 45-56.

Ku H, Chen JJ, Hu M, et al. 2022. Myopia Development in Tree Shrew Is Associated with Chronic Inflammatory Reactions. *Curr Issues Mol Biol*, **44**(9): 4303-4313.

Laverne G, Pesce J, Reynders A, et al. 2022. Cholinergic interneuron inhibition potentiates corticostriatal transmission in direct medium spiny neurons and rescues motor learning in parkinsonism. *Cell Rep*, **40**(1): 111034.

Lee K, Holley SM, Shobe JL, et al. 2017. Parvalbumin Interneurons Modulate Striatal Output and Enhance Performance during Associative Learning. *Neuron*, **93**(6): 1451-1463 e1454.

Lehericy S, Hirsch EC, Cervera P, et al. 1989. Selective loss of cholinergic neurons in the ventral striatum of patients with Alzheimer disease. *Proc Natl Acad Sci U S A*, **86**(21): 8580-8584.

Li CJ, Hui YQ, Zhang R, et al. 2023. A comparison of behavioral paradigms assessing spatial memory in tree shrews. *Cereb Cortex*, **33**(19): 10303-10321.

Li H, Xiang BL, Li X, et al. 2024. Cognitive Deficits and Alzheimer's Disease-Like Pathologies in the Aged Chinese Tree Shrew. *Mol Neurobiol*, **61**(4): 1892-1906.

Li X, Yu B, Sun Q, et al. 2018. Generation of a whole-brain atlas for the cholinergic system and mesoscopic projectome analysis of basal forebrain cholinergic neurons. *Proc Natl Acad Sci U S A*, **115**(2): 415-420.

Liebrand M, Karabanov A, Antonenko D, et al. 2020. Beneficial effects of cerebellar tDCS on motor learning are associated with altered putamen-cerebellar connectivity: A simultaneous tDCS-fMRI study. *Neuroimage*, **223**: 117363.

Lin CP, Frigerio I, Boon BDC, et al. 2022. Structural (dys)connectivity associates with cholinergic cell density in Alzheimer's disease. *Brain*, **145**(8): 2869-2881.

Luchicchi A, Bloem B, Viana JN, et al. 2014. Illuminating the role of cholinergic signaling in circuits of attention and emotionally salient behaviors. *Front Synaptic Neurosci*, **6**: 24.

Maher EE, Prillaman ME, Keskinoz EN, et al. 2021. Immunocytochemical and ultrastructural organization of the taste thalamus of the tree shrew (Tupaia belangeri). *J Comp Neurol*, **529**(10): 2558-2575.

Mason WT, Ho YW, Eckenstein F, et al. 1983. Mapping of cholinergic neurons associated with rat supraoptic nucleus: combined immunocytochemical and histochemical identification. *Brain Res Bull*, **11**(5): 617-626.

Maurice N, Liberge M, Jaouen F, et al. 2015. Striatal Cholinergic Interneurons Control Motor Behavior and Basal Ganglia Function in Experimental Parkinsonism. *Cell Rep*, **13**(4): 657-666.

Mesulam MM, Mufson EJ, Levey AI, et al. 1984. Atlas of cholinergic neurons in the forebrain and upper brainstem of the macaque based on monoclonal choline acetyltransferase immunohistochemistry and acetylcholinesterase histochemistry. *Neuroscience*, **12**(3): 669-686.

Nakano Y, Karube F, Hirai Y, et al. 2018. Parvalbumin-producing striatal interneurons receive excitatory inputs onto proximal dendrites from the motor thalamus in male mice. *J Neurosci Res*, **96**(7): 1186-1207.

Ni KM, Hou XJ, Yang CH, et al. 2016. Selectively driving cholinergic fibers optically in the thalamic reticular nucleus promotes sleep. *Elife*, **5**.

Ni RJ, Huang ZH, Luo PH, et al. 2018a. The tree shrew cerebellum atlas: Systematic nomenclature, neurochemical characterization, and afferent projections. *J Comp Neurol*, **526**(17): 2744-2775.

Ni RJ, Huang ZH, Shu YM, et al. 2018b. Atlas of the Striatum and Globus Pallidus in the Tree Shrew: Comparison with Rat and Mouse. *Neurosci Bull*, **34**(3): 405-418.

Ni RJ, Shu YM, Li T, et al. 2021. Whole-Brain Afferent Inputs to the Caudate Nucleus, Putamen, and Accumbens Nucleus in the Tree Shrew Striatum. *Front Neuroanat*, **15**: 763298.

Nishijo T, Suzuki E, Momiyama T. 2022. Serotonin 5-HT(1A) and 5-HT(1B) receptor-mediated inhibition of glutamatergic transmission onto rat basal forebrain cholinergic neurones. *J Physiol*, **600**(13): 3149-3167.

Okada K, Nishizawa K, Fukabori R, et al. 2014. Enhanced flexibility of place discrimination learning by targeting striatal cholinergic interneurons. *Nat Commun*, **5**: 3778.

Pan TT, Liu C, Li DM, et al. 2022. Nucleus accumbens-linked executive control networks mediating reversal learning in tree shrew brain. *Zool Res*, **43**(4): 528-531.

Picciotto MR, Higley MJ, Mineur YS. 2012. Acetylcholine as a neuromodulator: cholinergic signaling shapes nervous system function and behavior. *Neuron*, **76**(1): 116-129.

Prensa L, Richard S, Parent A. 2003. Chemical anatomy of the human ventral striatum and adjacent basal forebrain structures. *J Comp Neurol*, **460**(3): 345-367.

Raghanti MA, Stimpson CD, Marcinkiewicz JL, et al. 2008. Cholinergic innervation of the frontal cortex: differences among humans, chimpanzees, and macaque monkeys. *J Comp Neurol*, **506**(3): 409-424.

Rice MW, Roberts RC, Melendez-Ferro M, et al. 2011. Neurochemical characterization of the tree shrew dorsal striatum. *Front Neuroanat*, **5**: 53.

Ruan P, Yang C, Su J, et al. 2013. Histopathological changes in the liver of tree shrew (Tupaia belangeri chinensis) persistently infected with hepatitis B virus. *Virol J*, **10**: 333.

Salisbury DF, Wang Y, Yeh FC, et al. 2021. White Matter Microstructural Abnormalities in the Broca's-Wernicke's-Putamen "Hoffman Hallucination Circuit" and Auditory Transcallosal Fibers in First-Episode Psychosis With Auditory Hallucinations. *Schizophr Bull*, **47**(1): 149-159.

Sarter M, Lustig C, Blakely RD, et al. 2016. Cholinergic genetics of visual attention: Human and mouse choline transporter capacity variants influence distractibility. *J Physiol Paris*, **110**(1-2): 10-18.

Satchell M, Butel-Fry E, Noureddine Z, et al. 2025. Cholinergic modulation of neural networks supports sequential and complementary roles for NREM and REM states in memory consolidation. *PLoS Comput Biol*, **21**(6): e1013097.

Schehka S & Zimmermann E. 2009. Acoustic features to arousal and identity in disturbance calls of tree shrews (Tupaia belangeri). *Behav Brain Res*, **203**(2): 223-231.

Shekari A & Fahnestock M. 2021. Cholinergic neurodegeneration in Alzheimer disease mouse models. *Handb Clin Neurol*, **182**: 191-209.

Smeets WJ, Marin O, Gonzalez A. 2000. Evolution of the basal ganglia: new perspectives through a comparative approach. *J Anat*, **196 (Pt 4)**(Pt 4): 501-517.

Spruston N. 2008. Pyramidal neurons: dendritic structure and synaptic integration. *Nat Rev Neurosci*, **9**(3): 206-221.

Tago H, Mcgeer PL, Bruce G, et al. 1987. Distribution of choline acetyltransferase-containing neurons of the hypothalamus. *Brain Res*, **415**(1): 49-62.

Van Hasselt SJ, Epifani L, Zantinge D, et al. 2023. A Study on REM Sleep Homeostasis in the Day-Active Tree Shrew (Tupaia belangeri): Cold-Induced Suppression of REM Sleep Is Not Followed by a Rebound. *Biology (Basel)*, **12**(4).

Vostrikov VM & Uranova NA. 2020. Reduced density of oligodendrocytes and oligodendrocyte clusters in the caudate nucleus in major psychiatric illnesses. *Schizophr Res*, **215**: 211-216.

Wang H, Zhu Q, Ding L, et al. 2019. Scalable volumetric imaging for ultrahigh-speed brain mapping at synaptic resolution. *Natl Sci Rev*, **6**(5): 982-992.

Wang L, Lu J, Yang Y, et al. 2023. Mechanism of cognitive impairment induced by d-galactose and l-glutamate through gut-brain interaction in tree shrews. *Synapse*, **77**(5): e22274.

Wang YT, Xu QQ, Wang SW, et al. 2025. Anatomical mapping of GFAP-immunoreactive astrocytes in the tree shrew brain. *Zool Res*, **46**(4): 877-892.

Williams VM, Bhagwandin A, Swiegers J, et al. 2022a. Distribution of cholinergic neurons in the brains of a lar gibbon and a chimpanzee. *Anat Rec (Hoboken)*, **305**(6): 1516-1535.

Williams VM, Bhagwandin A, Swiegers J, et al. 2022b. Distribution of cholinergic neurons in the brains of a lar gibbon and a chimpanzee. *Anat Rec (Hoboken)*, **305**(6): 1516-1535.

Woolf NJ, Eckenstein F, Butcher LL. 1984. Cholinergic systems in the rat brain: I. projections to the limbic telencephalon. *Brain Res Bull*, **13**(6): 751-784.

Xu M, Kobets A, Du JC, et al. 2015. Targeted ablation of cholinergic interneurons in the dorsolateral striatum produces behavioral manifestations of Tourette syndrome. *Proc Natl Acad Sci U S A*, **112**(3): 893-898.

Yao YG, Lu L, Ni RJ, et al. 2024. Study of tree shrew biology and models: A booming and prosperous field for biomedical research. *Zool Res*, **45**(4): 877-909.

Ye MS, Zhang JY, Yu DD, et al. 2021. Comprehensive annotation of the Chinese tree shrew genome by large-scale RNA sequencing and long-read isoform sequencing. *Zool Res*, **42**(6): 692-709.

Zeng H & Sanes JR. 2017. Neuronal cell-type classification: challenges, opportunities and the path forward. *Nat Rev Neurosci*, **18**(9): 530-546.

Zhang J, Luo RC, Man XY, et al. 2020. The anatomy of the skin of the Chinese tree shrew is very similar to that of human skin. *Zool Res*, **41**(2): 208-212.

Zhang R, Long JL, Ye YF, et al. 2025. Distributions of parvalbumin, calbindin-D28k, and calretinin in the cerebrum of Chinese tree shrews (Tupaia belangeri chinensis): A high-resolution neuroanatomical resource. *Zool Res*, **46**(4): 893-911.

Zhao Y, Kirschenhofer T, Harvey M, et al. 2024. Mediodorsal thalamus and ventral pallidum contribute to subcortical regulation of the default mode network. *Commun Biol*, **7**(1): 891.

Zheng W, An Y, Li K, et al. 2025. Self-supervised learning analysis of multi-FISH labeled cell-type map in thick brain slices. *Front Neurosci*, **19**: 1622950.

Zhou J-N & Rong-Jun N. 2016. The Tree Shrew (Tupaia belangeri chinensis) Brain in Stereotaxic Coordinates. Pages 1 online resource (XIII, 588 pages 557 illustrations, 280 illustrations in color. 1st ed. Springer Singapore : Imprint: Springer,, Singapore.

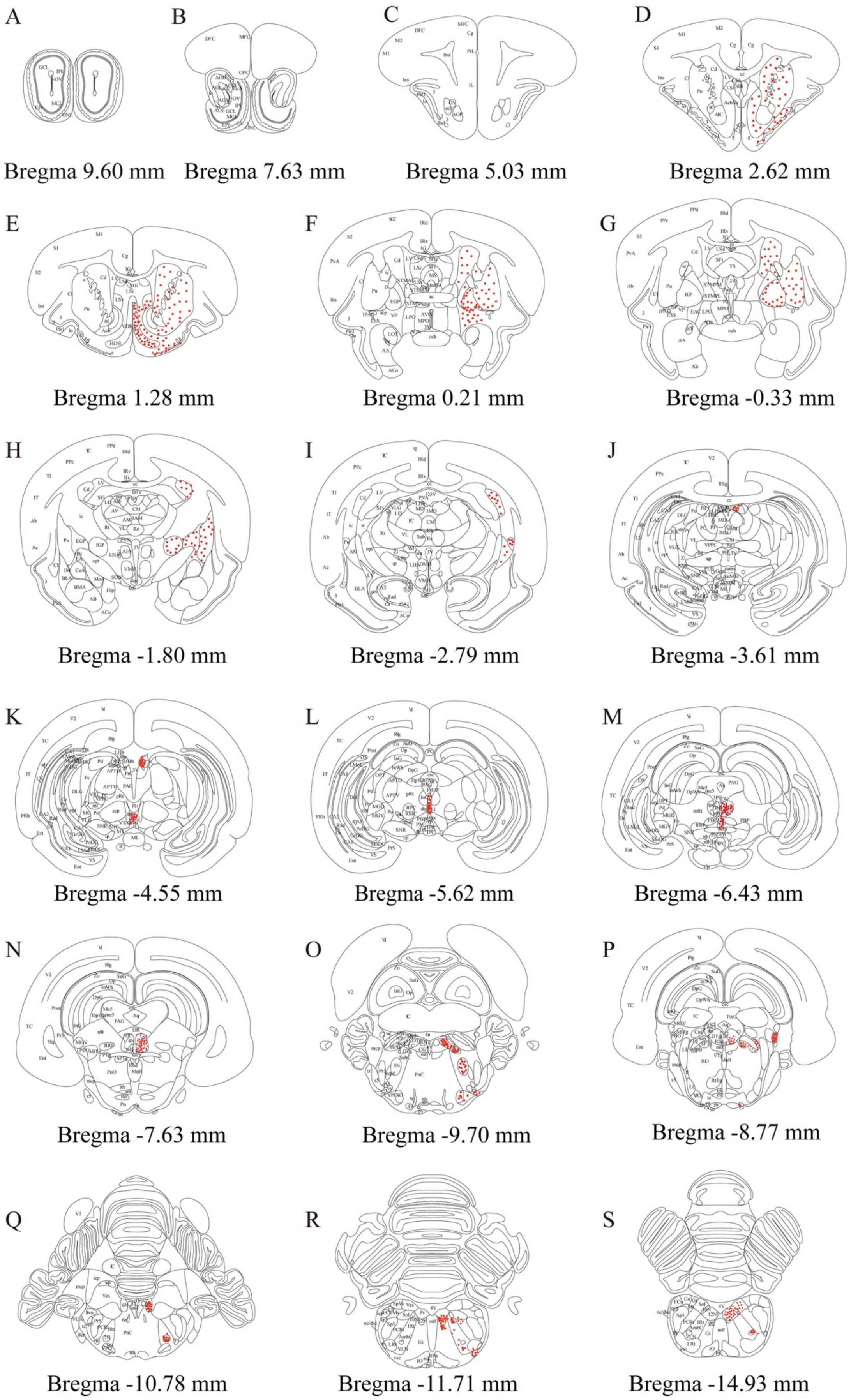

A Bregma 9.60 mm

B Bregma 7.63 mm

C Bregma 5.03 mm

D Bregma 2.62 mm

E Bregma 1.28 mm

F Bregma 0.21 mm

G Bregma -0.33 mm

H Bregma -1.80 mm

I Bregma -2.79 mm

J Bregma -3.61 mm

K Bregma -4.55 mm

L Bregma -5.62 mm

M Bregma -6.43 mm

N Bregma -7.63 mm

O Bregma -9.70 mm

P Bregma -8.77 mm

Q Bregma -10.78 mm

R Bregma -11.71 mm

S Bregma -14.93 mm

Figure 1: The distribution of ChAT-ir neurons in coronal sections of tree shrews. Schematic drawings of 19 coronal sections (A–S), arranged from rostral to caudal with reference to the bregma, were presented. Red dots indicate the distribution of ChAT-ir neuronal soma. Dot density reflects the relative abundance of immunoreactive cells in the corresponding brain regions.

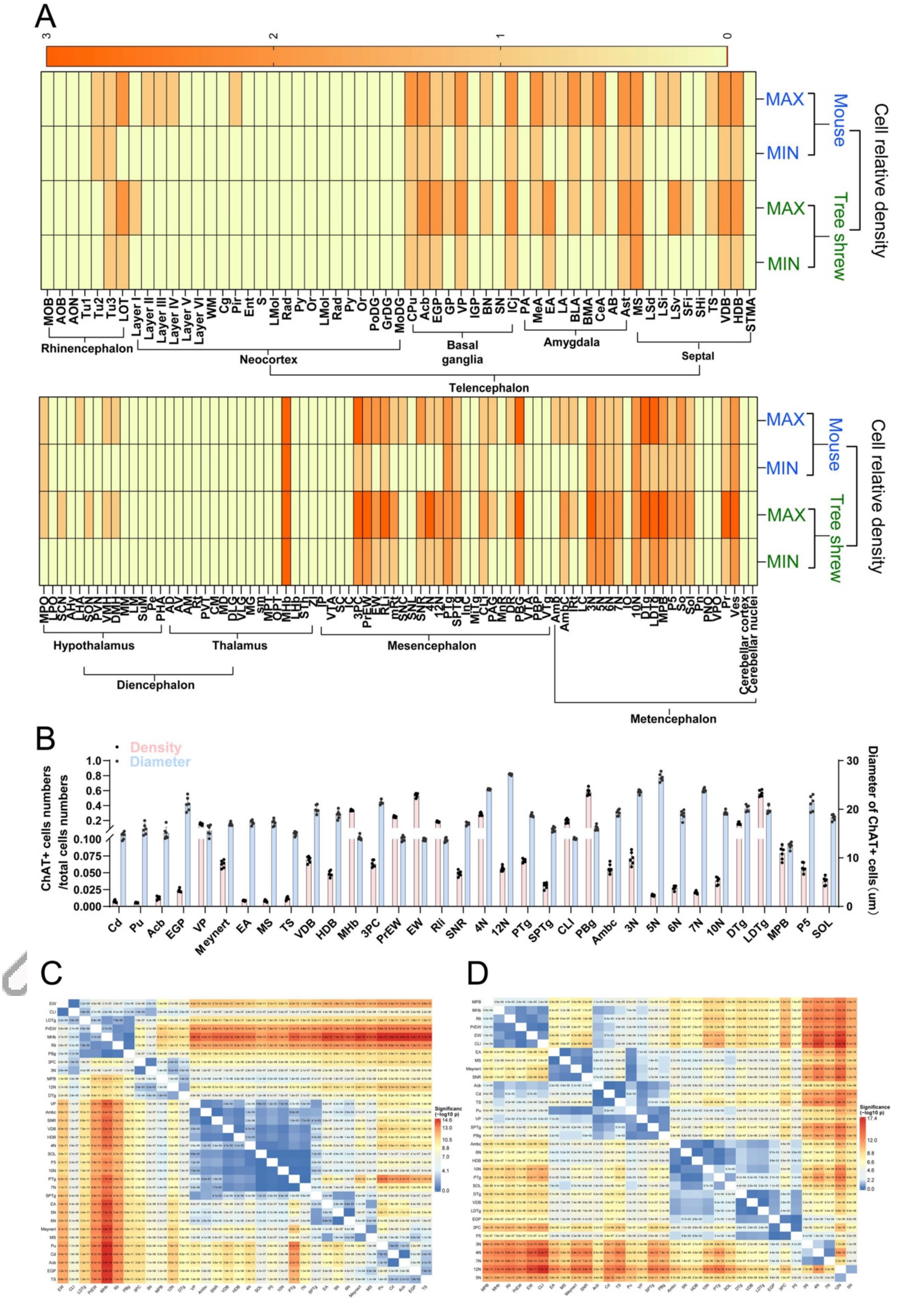
A
3
2
1
0
MAX
MIN
MAX
MIN
Mouse
Tree shrew
Cell relative density
MOB AOB AON Tu1 Tu2 Tu3 LOT Layer I Layer II Layer III Layer IV Layer V Layer VI WM Cg Pir Ent S LMol Rad Py Or LMol Rad Py Or PoDG GrDG MoDG CPu Acb EGP GP VP IGP BN SN ICj PA MeA EA LA BLA BMA CeA AB Ast MS LSd LSi LSv SFi SHi TS VDB HDB STMA
Rhinencephalon
Neocortex
Basal ganglia
Amygdala
Septal
Telencephalon
MPO LPO SCN AHy LHA SON PVN VMH DMH MM LM SuM Pe PH AD AV AM Rt PVT CM MD DLG VLG MG sm MPT MHb LHb STh ZI VTA SC IC 3PC PrEW EW mRt SNC SNL SNR Rli 4N 12N SPTg MiTg InC CLi PAG MnR DR PBG VTg PBP Ambc Amb IRt LC 3N 5N 6N 7N 10N IO DTg LDTg MPB P5 So Sol Pn PnO VPO Pr Ves Cerebellar cortex Cerebellar nuclei
Hypothalamus
Thalamus
Mesencephalon
Diencephalon
Metencephalon
B
Density
Diameter
ChAT+ cells numbers /total cells numbers
1.0
0.8
0.6
0.4
0.2
0.100
0.075
0.050
0.025
0.000
Diameter of ChAT+ cells (um)
30
20
10
0
Cd Pu Acb EGP VP Meynert EA MS TS VDB HDB MHb 3PC PrEW EW Rli SNR 4N 12N PTg SPTg CLI PBg Ambc 3N 5N 6N 7N 10N DTg LDTg MPB P5 SOL
C
Significance (−log10 p)
14.6
13.0
10.5
8.8
7.0
4.1
0.0
D
Significance (−log10 p)
17.4
12.0
8.8
6.6
4.6
2.2
0.0

Figure 2: Density and diameter of ChAT-ir neurons in different nuclei of tree shrews and mice.

The color of each box represented the relative density of ChAT-ir in the brain nuclei, as 0-none, 1-sparse, 2-moderate, 3-dense for ChAT-ir staining (A). The minimum (Min) and maximum (Max) values indicate the range of densities in coronal slices. Density and diameter of ChAT-ir neurons in the tree shrews (B). The left vertical axis shows the ChAT$^+$ cells numbers / total cells numbers (red), the right vertical axis shows their mean soma diameter (blue), and the horizontal axis shows the nuclei containing ChAT-ir neurons (n=6). Results are expressed as mean ± SD. Pairwise comparison heatmaps showing the statistical significance of the density (C) and soma diameter (D) of ChAT-ir neurons across different nuclei in the tree shrew. Different color indicates the level of statistical significance. Numerical values within the squares denote the corresponding P values. Three adult male tree shrews (8 months) and three male mice (8-10 weeks) were used in this study.

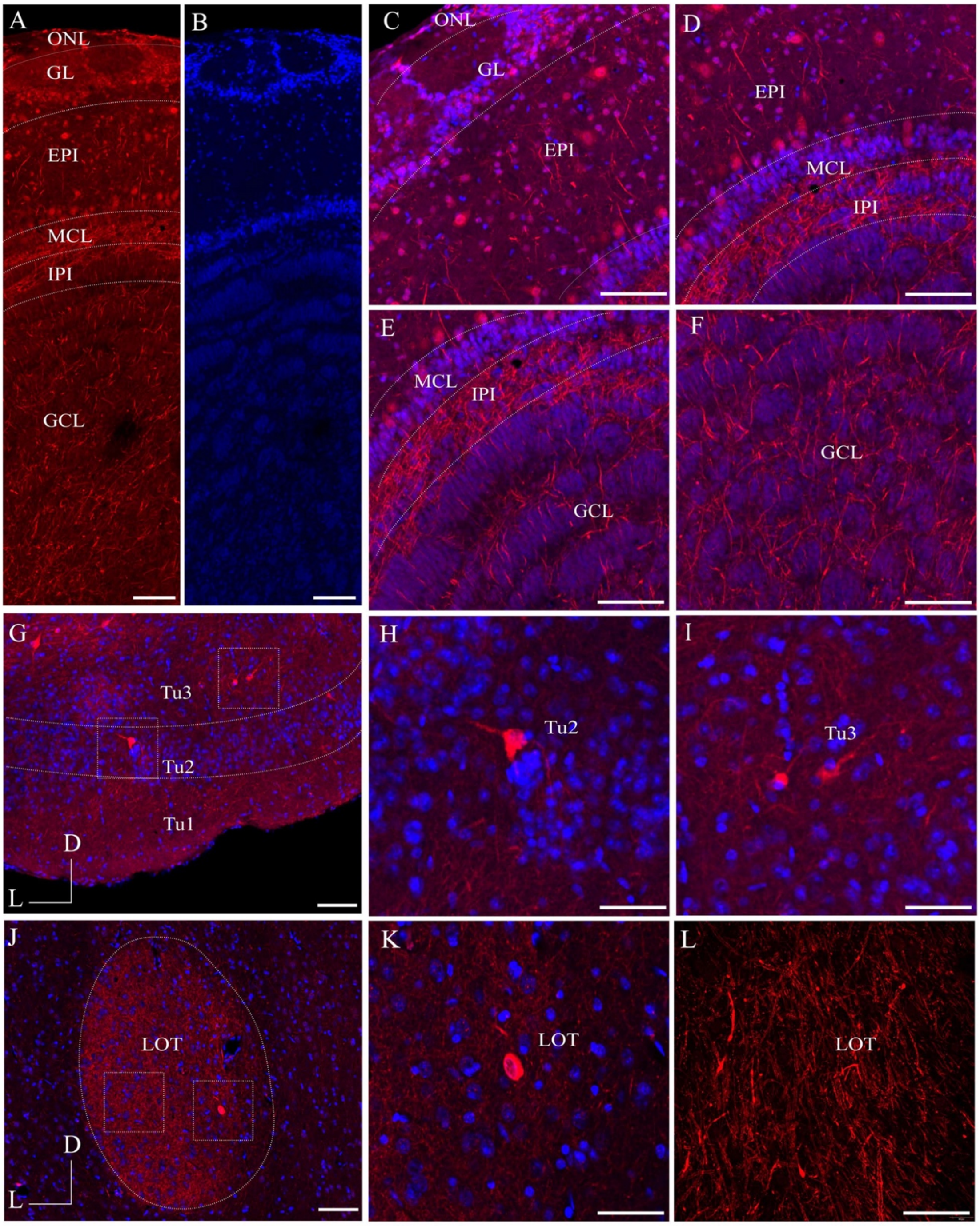

Figure 3: Distribution of ChAT-ir neurons in the rhinencephalon of tree shrews.

The MOB (A, B), Tu (G), and LOT (J) of tree shrews were illustrated by ChAT immunofluorescence staining. Magnified pictures (C– F: layers in MOB; H: Tu2; I: Tu3; K: neuron in LOT and L: fibers in LOT) were also presented. The cross lines in G and J indicate orientation (D, dorsal; L, lateral). Scale bars: A, B, G, J, 100 μm; C, D, E, F, H, I, K, 50 µm; L, 10 µm. Three adult male tree shrews (8 months) were used in this study.

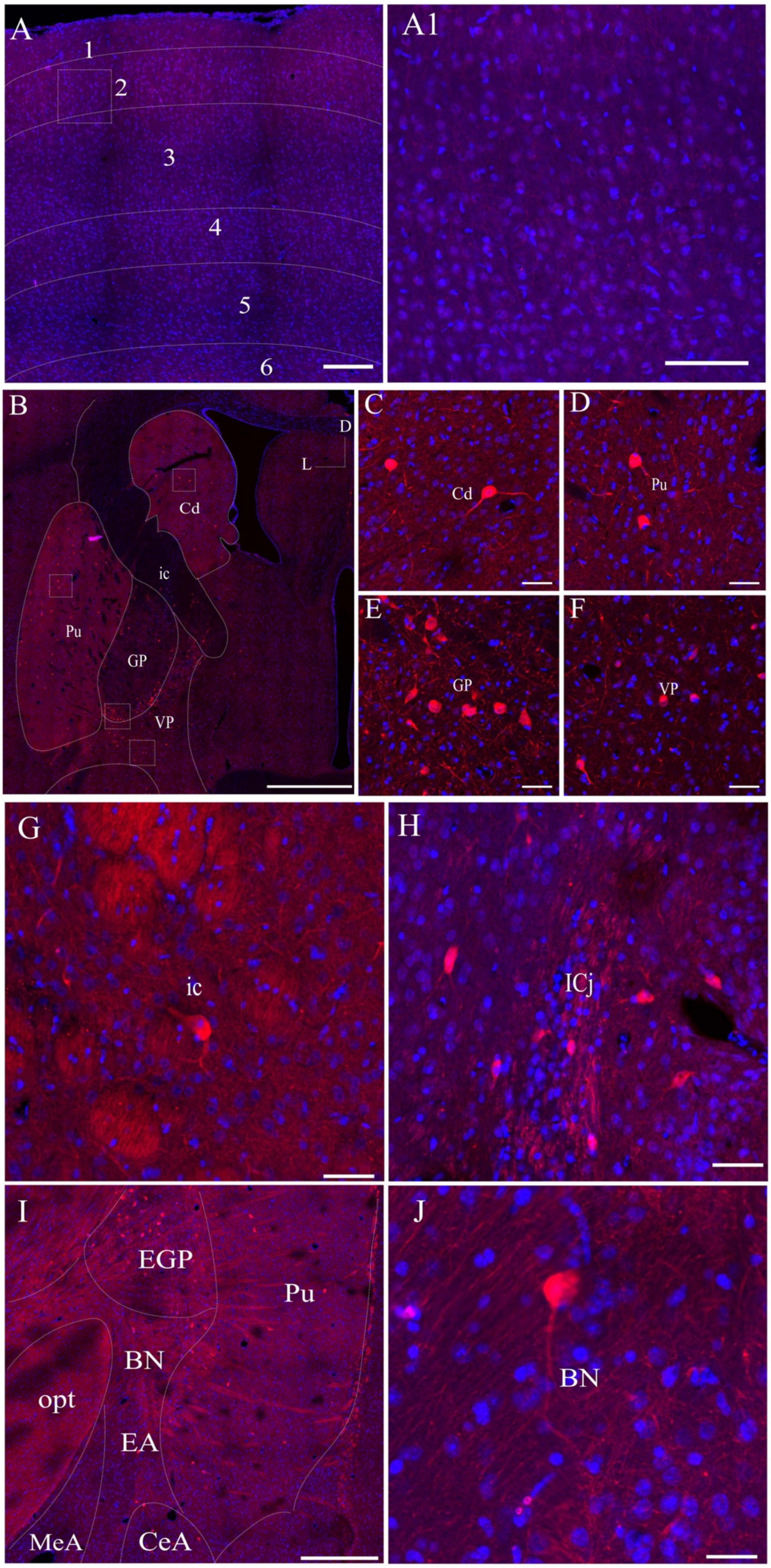
A
1
2
3
4
5
6
A1
B
D
L
Cd
ic
Pu
GP
VP
C
Cd
D
Pu
E
GP
F
VP
G
ic
H
ICj
I
EGP
Pu
BN
opt
EA
MeA
CeA
J
BN

Figure 4: Distribution of ChAT-ir neurons in neocortex and basal ganglia of tree shrews.

Immunofluorescence staining of neocortex (A, A1) and basal ganglia (B) in tree shrews were presented. The magnified view of Layer 2 of cortex (A1), Cd (C), Pu (D), GP (E), VP (F), ic (G), ICj (H), and BN (I, J) in tree shrews. Scale bars: A, 200 µm; B, 1000 µm; I, 500 µm; A1, C, D, E, F, G, H, J, 50 µm. Three adult male tree shrews (8 months) and three male mice (8-10 weeks) were used in this study.

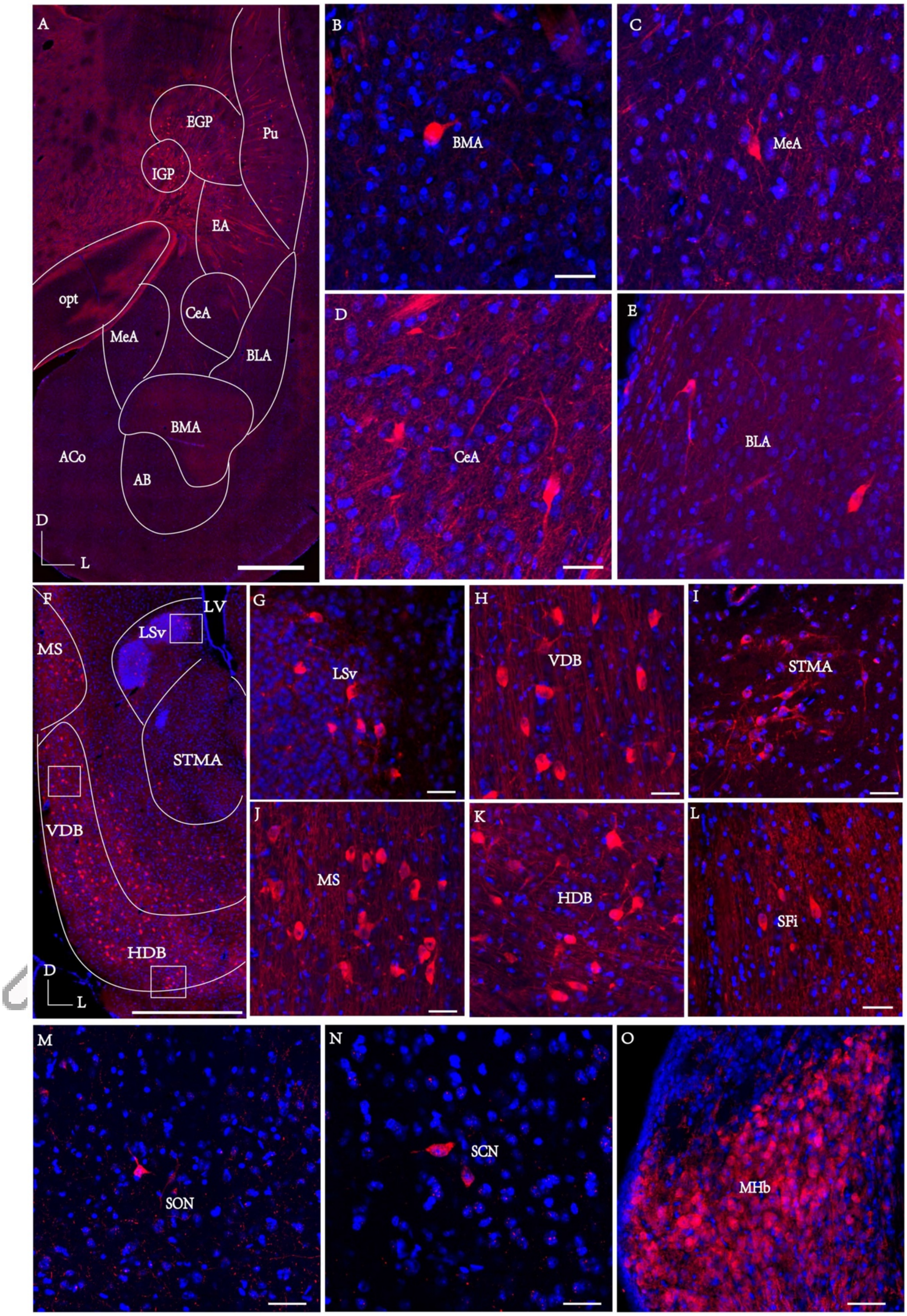
A
EGP
Pu
IGP
EA
opt
CeA
MeA
BLA
BMA
ACo
AB
D
L
B
BMA
C
MeA
D
CeA
E
BLA
F
LV
LSv
MS
STMA
VDB
HDB
D
L
G
LSv
H
VDB
I
STMA
J
MS
K
HDB
L
SFi
M
SON
N
SCN
O
MHb

Figure 5: Distribution of ChAT-ir neurons in amygdala, septal, preoptic regions and diencephalon of tree shrews.

Immunofluorescence staining of amygdala (A) in tree shrews, including BMA (B), MeA (C), CeA (D) and BLA (E) were presented. Immunofluorescence staining of septal and preoptic regions in tree shrews, including LSv (G), STMA (I) and SFi (L) were presented. The immunofluorescence staining of medial septum/diagonal band complex (F) in tree shrews, including VDB (H), MS (J), and HDB (K), were illustrated. The immunofluorescence staining of in diencephalon in tree shrews, including SON (M), SCN (N), and MHb (O) were illustrated. Scale bars: A, 1000 μm; F, 100 μm; B– E, G–O, 50 μm. Three adult male tree shrews (8 months) were used in this study.

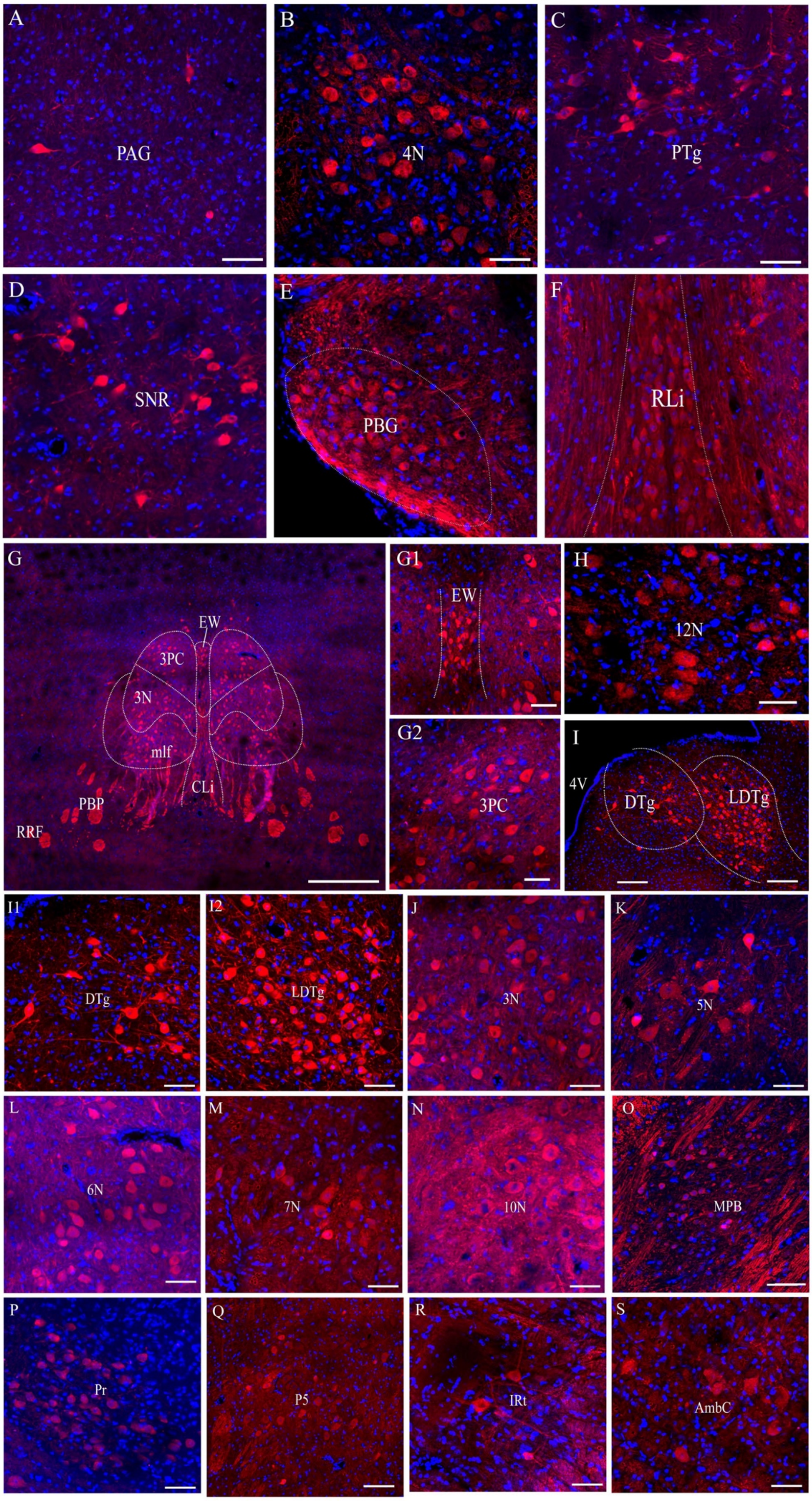
A
PAG
B
4N
C
PTg
D
SNR
E
PBG
F
RLi
G
EW
3PC
3N
mlf
CLi
PBP
RRF
G1
EW
H
12N
G2
3PC
I
4V
DTg
LDTg
I1
DTg
I2
LDTg
J
3N
K
5N
L
6N
M
7N
N
10N
O
MPB
P
Pr
Q
P5
R
IRt
S
AmbC

Figure 6: Distribution of ChAT-ir neurons in mesencephalon and metencephalon of tree shrews.

Immunofluorescence staining of mesencephalon in tree shrews, including PAG (A), 4N (B), PTG (C), SNR (D), PBG (E), Rli (F), EW (G, G1), 3PC (G, G2), 12N (H) were presented. Immunofluorescence staining of metencephalon in tree shrews, including DTg (I, I1), LDTg (I, I2), 3N (J), 5N (K), 6N (L), 7N (M), 10N (N), MPB (O), Pr (P), P5 (Q), IRt (R), AmbC (S) were presented. Scale bars: A-F, G1– G2, H, I1– I2, J– S, 50 µm; G, 500 µm; I, 100 µm. Three adult male tree shrews (8 months) were used in this study.

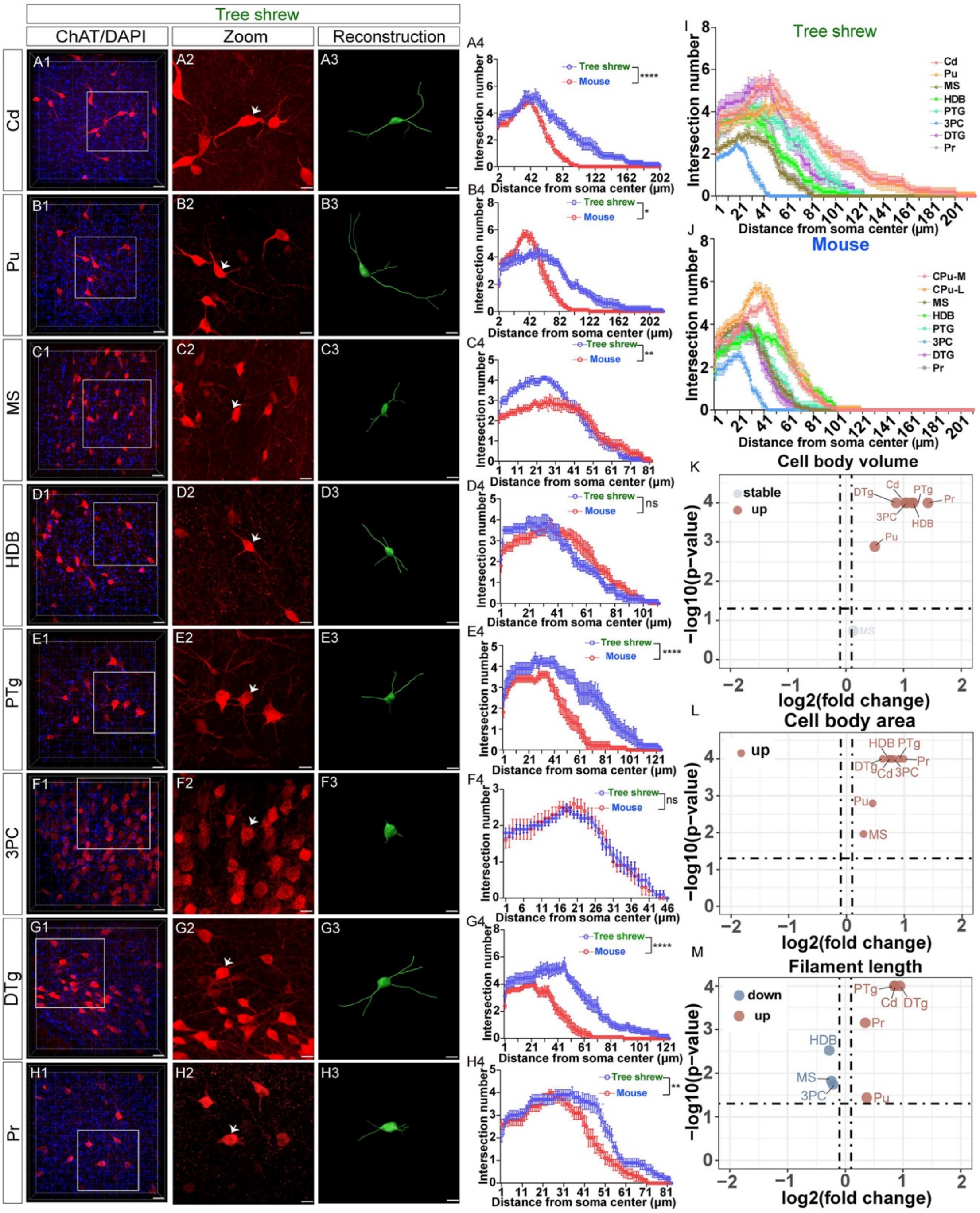

Figure 7: Morphological analysis in three dimensions of ChAT-ir neurons of tree shrew.

ChAT immunostaining of Cd (A1), Pu (B1), MS (C1), HDB (D1), PTg (E1), 3PC (F1), DTg (G1) and Pr (H1) were presented. The corresponding magnified views (A2-H2) and three dimensions reconstructions (green) of neurons in each brain regions (A3-H3) were also provided. Sholl analyses of ChAT-ir neuron morphology in the tree shrews and mice were presented (A4-H4). Data are shown as the mean ± SEM. For A4-H4, two-way repeated measures ANOVA, main effect of species, *: $P<0.05$, **: $P<0.01$, ***: $P<0.001$, ****: $P<0.0001$. For both Tree shrew and mouse (n = 12 cells per brain region). Sholl analyses of ChAT-ir neuron morphology across different nuclei in the tree shrew (I) and mouse (J) were shown. Comparations of cell body volume (K), cell body area (L), process length (M) between tree shrews and mouse were illustrated by volcano plot. P values < 0.05 and absolute $\log_2$(fold change) values > 0.2 were considered statistically significant. Scale bars: A1–H1, 50 µm; A2–H2 and A3–H3, 20 µm. Three adult male tree shrews (8 months) and three male mice (8-10 weeks) were used in this study.

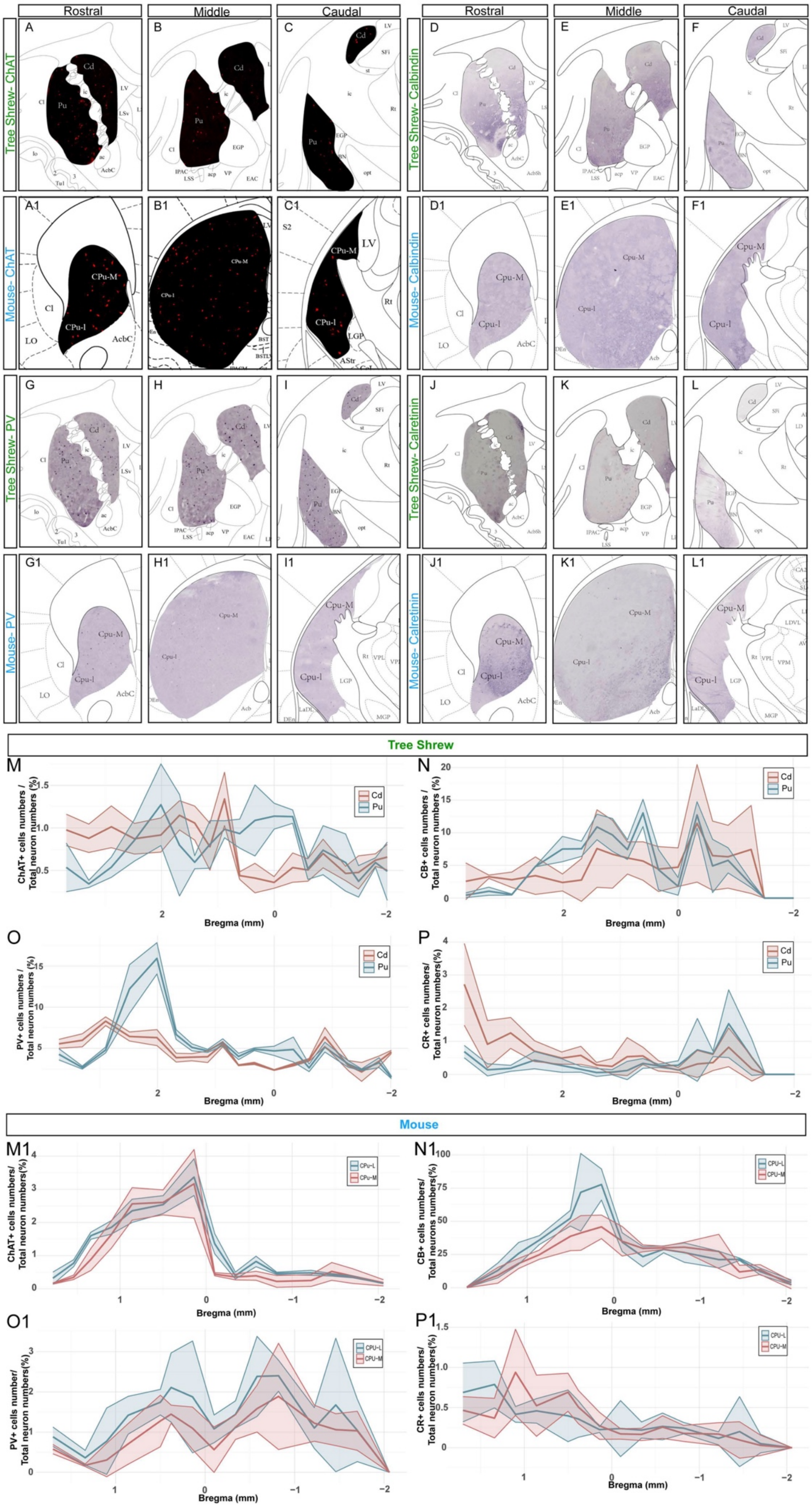
Rostral
Middle
Caudal
Rostral
Middle
Caudal
Tree Shrew- ChAT
Mouse- ChAT
Tree Shrew- Calbindin
Mouse- Calbindin
Tree Shrew- PV
Mouse- PV
Tree Shrew- Calretinin
Mouse- Calretinin
A
B
C
D
E
F
A1
B1
C1
D1
E1
F1
G
H
I
J
K
L
G1
H1
I1
J1
K1
L1
Cd
Pu
CPu-M
CPu-l
Cpu-M
Cpu-l
Tree Shrew
M
ChAT+ cells numbers / Total neuron numbers (%)
N
CB+ cells numbers / Total neuron numbers (%)
O
PV+ cells numbers / Total neuron numbers (%)
P
CR+ cells numbers/ Total neuron numbers(%)
Cd
Pu
Bregma (mm)
Mouse
M1
ChAT+ cells numbers/ Total neuron numbers(%)
N1
CB+ cells numbers/ Total neurons numbers(%)
O1
PV+ cells number/ Total neuron numbers(%)
P1
CR+ cells numbers/ Total neuron numbers(%)
CPu-L
CPu-M
Bregma (mm)

Figure 8: Distribution and mean density of interneurons in dorsal striatum from rostral to caudal.

The rostral (A, A1), middle (B, B1), and caudal (C, C1) distributions of ChAT‑ir neurons in the Cd and Pu of tree shrew, as well as in the Cpu‑M and Cpu‑L of mouse, were presented. The rostral (D, D1), middle (E, E1), and caudal (F, F1) distributions of CB neurons in the Cd and Pu of tree shrew, as well as in the Cpu‑M and Cpu‑L of mouse, were presented. The rostral (G, G1), middle (H, H1), and caudal (I, I1) distributions of PV neurons in the Cd and Pu of tree shrew, as well as in the Cpu‑M and Cpu‑L of mouse, were presented. The rostral (J, J1), middle (K, K1), and caudal (L, L1) distributions of CR neurons in the Cd and Pu of tree shrew, as well as in the Cpu‑M and Cpu‑L of mouse, were presented. The ChAT$^+$, CB$^+$, PV$^+$ and CR$^+$ cells / total cells numbers in dorsal striatum from rostral to caudal were calculated for tree shrew (M– P) and mouse (M1– P1). The shadow areas refer to the 95% corresponding confidence interval. Three adult male tree shrews (8 months) and three male mice (8-10 weeks) were used in this study.

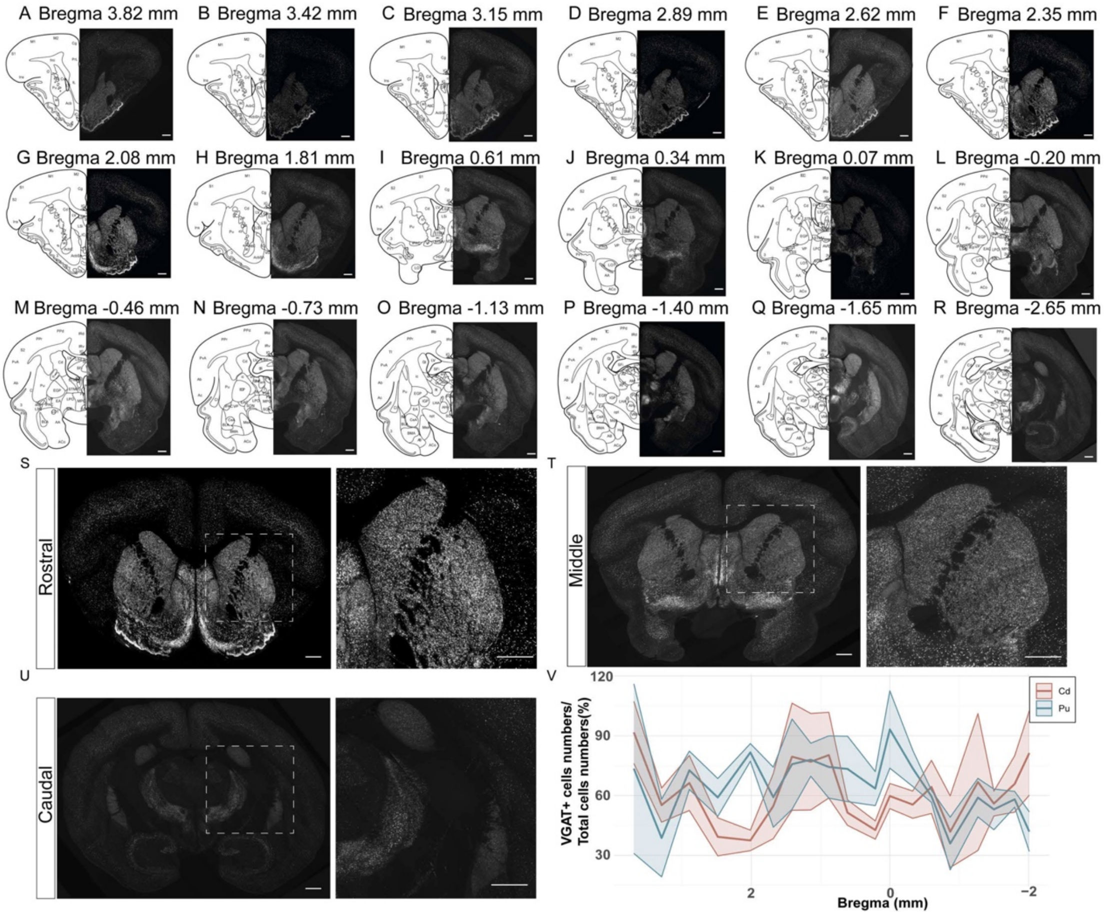

Figure 9: Distribution and mean density of Vgat neurons in dorsal striatum from rostral to caudal.

Representative images of Vgat neurons in the dorsal striatum of tree shrew brain from rostral to caudal (A– R) were presented. Representative magnified images of the rostral (S), middle (T), and caudal (U) distributions of Vgat neurons in the Cd and Pu of tree shrew were shown. The Vgat$^+$ neurons numbers / total cells numbers dorsal striatum from rostral to caudal were calculated for tree shrew (V). The shadow areas refer to the 95% corresponding confidence interval. Scale bars: A– U, 1000 µm. Three adult male tree shrews (8 months) were used in this study.

Table1: Density of ChAT-ir neurons in each brain region of tree shrews and mice.

Density of ChAT-ir cells in each brain region of tree shrews and mice. Brain regions in which ChAT immunoreactivity was detected are listed. Minimum (Min) and maximum (Max) values indicate the density range in each region across all animals examined. Symbols denote relative density: '–' = no ChAT-ir staining; '+' = sparse; '++' = moderate; '+++' = dense. Immunohistochemical analyses were conducted on three control tree shrews and three control mice. Three adult male tree shrews (8 months) and three male mice (8-10 weeks) were used in this study.

	Tree shrew		**Mouse**	
	Cell relative density		**Cell relative density**	
Brain region	**Min**	**Max**	**Min**	**Max**
Rhinencephalon	-	-	-	-
Main olfactory bulb (MOB)	-	-	-	-
Accessory olfactory bulb (AOB)	-	-	-	-
Anterior olfactory nucleus (AON)	-	-	-	-
Olfactory tubercle (Tu)				
Layer 1 of olfactory tubercle (Tu1)	-	-	-	-
Layer 2 of olfactory tubercle (Tu2)	-	+	-	+
Layer 3 of olfactory tubercle (Tu3)	+	++	+	+
Nucleus of the lateral olfactory tract (LOT)	+	+	+	++
Telencephalon				

Neocortex				
Layer 1	-	-	-	-
Layer 2	-	-	-	+
Layer 3	-	-	-	+
Layer 4	-	-	-	+
Layer 5	-	-	-	-
Layer 6	-	-	-	-
White matter (WM)	-	-	-	-
Cingulate cortex (Cg)	-	-	-	-
Piriform cortex (Pir)	-	-	-	+
Entorhinal cortex (Ent)	-	-	-	-
Subiculum (S)	-	-	-	-
Hippocampus				
CA1	-	-	-	-
Lacunosum moleculare layer (LMol)	-	-	-	-
Radiatum layer (Rad)	-	-	-	-
Pyramidal cell layer (Py)	-	-	-	-
Oriens layer (Or)	-	-	-	-
CA3				
Lacunosum moleculare layer (LMol)	-	-	-	-
Radiatum layer (Rad)	-	-	-	-
Pyramidal cell layer (Py)	-	-	-	-
Dentate gyrus	-	-	-	-
Polymorph cell layer (PoDG)	-	-	-	-

Granular cell layer (GrDG)	-	-	-	-
Molecular cell layer (MoDG)	-	-	-	-
Basal ganglia				
Striatum (Caudate putamen) (CPu)	+	+	+	++
Accumbens nucleus (Acb)	+	++	+	++
External globus pallidus (EGP)	+	++	+	+
Globus pallidus (GP)	-	+	-	+
Ventral pallidum (VP)	+	++	+	++
Internal globus pallidus (IGP)	-	-	-	-
Basal nucleus (Meynert) (BN)	-	+	-	+
Substantia nigra (SN)	-	-	-	-
Islands of Calleja (ICj)	+	++	+	++
Amygdala				
Periamygdaloid cortex (PA)	-	-	-	-
Medial amygdaloid nucleus (MeA)	-	+	+	++
Sublenticular extended amygdala (EA)	+	++	-	+
Lateral amygdaloid nucleus (LA)	-	-	-	+
Basolateral amygdaloid nucleus (BLA)	-	+	+	++
Basomedial amygdaloid nucleus (BMA)	-	-	-	+
Central amygdaloid nucleus (CeA)	-	+	+	++
Accessory basal nucleus (AB)	-	-	-	-
Amygdalostriatal transition area (Ast)	+	++	+	++
Septal				
Medial septal nucleus (MS)	++	++	+	++

Lateral septal nucleus (LS)				
Dorsal part (LSd)	-	-	-	-
Intermediate part (LSi)	-	-	-	+
Ventral part (LSv)	-	++	-	+
Septofi mbrial nucleus (SFi)	-	+	-	-
Septohippocampal nucleus (SHi)	-	-	-	-
Triangular septal nucleus (TS)	-	+	-	+
Nucleus of the vertical limb of the diagonal band (VDB)	+	++	+	++
Nucleus of the horizontal limb of the diagonal band (HDB)	+	++	+	++
Bed nucleus of the stria terminalis, medial division, anterior part (STMA)	-	-	-	-
Diencephalon				
Hypothalamus				
Suprachiasmatic nucleus (SCN)	-	+	-	-
Anterior hypothalamic area (AHy)	-	-	-	-
Lateral hypothalamic area (LHA)	-	-	-	+
Supraoptic nucleus (SON)	-	+	-	-
Paraventricular hypothalamic nucleus (PVN)	-	-	-	-
Ventromedial hypothalamic nucleus (VMH)	-	+	-	+
Dorsomedial hypothalamic nucleus (DMH)	-	+	-	+
Medial mammillary nucleus (MM)	-	-	-	-
Lateral mammillary nucleus (LM)	-	-	-	-
Supramammillary nucleus (SuM)	-	-	-	-
Periventricular hypothalamic nucleus (Pe)	-	-	-	-
Posterior hypothalamic area (PHA)	-	-	-	-

Medial preoptic nucleus (MPO)	-	+	+	+
Lateral preoptic area (LPO)	-	-	-	-
Thalamus				
Anterodorsal thalamic nucleus (AD)	-	-	-	-
Anteroventral thalamic nucleus (AV)	-	-	-	-
Anteromedial thalamic nucleus (AM)	-	-	-	-
Reticular thalamic nucleus (Rt)	-	-	-	-
Paraventricular thalamic nucleus (PVT)	-	-	-	-
Central medial thalamic nucleus (CM)	-	-	-	-
Mediodorsal thalamic nucleus (MD)	-	-	-	-
Dorsal lateral geniculate nucleus (DLG)	-	-	-	-
Ventral lateral geniculate nucleus (VLG)	-	-	-	-
Medial geniculate nucleus (MG)	-	-	-	-
Nucleus of the stria medullaris (sm)	-	-	-	-
Pretectal nucleus				
Medial pretectal nucleus (MPT)	-	-	-	-
Olivary pretectal nucleus (OPT)	-	-	-	-
Medial habenular nucleus (MHb)	+++	+++	+++	+++
Lateral habenular nucleus (LHb)	-	-	-	-
Subthalamic nucleus (STh)	-	-	-	-
Zona incerta（ZI）	-	-	-	-
Mesencephalon				
Interpeduncular nucleus (IP)	-	-	-	-
Ventral tegmental area (VTA)	-	-	-	-

Superior colliculus (SC)	-	-	-	-
Inferior colliculus (IC)	-	-	-	-
Oculomotor nucleus, parvicellular part (3PC)	++	+++	+	+++
Pre-Edinger-Westphal nucleus (PrEW)	++	+++	+	++
Edinger-Westphal nucleus (EW)	+	++	-	++
Rostral linear nucleus of the raphe (RLi)	+	+++	+	++
Mesencephalic reticular formation (mRt)	+	++	-	+
Substantia nigra, compact part (SNC)	-	-	-	+
Substantia nigra, lateral part (SNL)	-	-	-	-
Substantia nigra, reticular part (SNR)	+	++	-	++
Trochlear nucleus (4N)	+	+++	-	+
Hypoglossal nucleus (12N)	+	++	-	+
Pedunculopontine tegmental nucleus (PTg)	++	++	++	++
Subpeduncular tegmental nucleus (SPTg)	+	++	+	+
Interstitial nucleus of Cajal (InC)	-	-	-	-
Microcellular tegmental nucleus (MiTg)	-	-	-	-
Caudal linear nucleus of the raphe (CLi)	+	++	+	+
Periaqueductal gray (PAG)	-	+	-	+
Median raphe nucleus (MnR)	-	-	-	-
Dorsal raphe nucleus (DR)	-	+	-	+
Parabigeminal nucleus (PBG)	++	+++	+	+++
Ventral tegmental area (VTA)	-	-	-	-
Parabrachial pigmented nucleus of the VTA (PBP)	-	-	-	-
Ventral tegmental nucleus (VTg)	-	-	-	-

Metencephalon/Myelencephalon				
Ambiguus nucleus (Amb)	-	-	-	+
Ambiguus nucleus, compact part (AmbC)	+	++	-	+
Intermediate reticular nucleus (IRt)	-	+	-	+
Locus coeruleus (LC)	-	-	-	-
Oculomotor nucleus (3N)	++	+++	++	++
Motor trigeminal nucleus (5N)	++	++	+	+
Abducens nucleus (6N)	++	++	+	+
Facial nucleus (7N)	+	++	+	+
Inferior olive (IO)	-	-	-	-
Dorsal motor nucleus of vagus (10N)	++	++	++	++
Dorsal tegmental nucleus (DTg)	+	+++	+	+++
Laterodorsal tegmental nucleus (LDTg)	++	+++	+	+++
Medial parabrachial nucleus (MPB)	++	+++	+	++
peritrigeminal zone (P5)	+	++	+	+
Superior olive (So)	+	++	+	++
Solitary nucleus (Sol)	+	++	+	+
Pontine nuclei (Pn)	-	-	-	-
Pontine reticular nucleus, oral part (PnO)	-	-	-	-
Ventral periolivary nucleus (VPO)	-	-	-	
Prepositus nucleus (Pr)	+	+++	+	+
Vestibular nucleus (Ves)	++	+++	++	++
Cerebellar cortex	-	-	-	-
Cerebellar nuclei	-	-	-	-

树鼩乙酰胆碱转移酶免疫阳性神经元表达全脑图谱以及与小鼠的比较

摘要

中枢胆碱能系统调控多种神经功能，包括学习、注意力、觉醒、睡眠、情绪调节及行为控制。作为灵长类动物的近缘进化物种，树鼩是神经生物学研究的重要模型。然而，其全脑中乙酰胆碱转移酶免疫阳性（ChAT-ir）神经元的解剖分布特征仍不明确。本研究通过 ChAT 免疫荧光标记技术，系统绘制了树鼩全脑 ChAT-ir 神经元的分布与形态，并与小鼠进行对比。在新皮层中，树鼩未检测到 ChAT-ir 神经元，而小鼠则呈现稀疏的皮层标记。对皮层下区域的半定量分析显示，总体分布基本保守，但树鼩的滑车核与前置核 ChAT-ir 神经元密度高于小鼠。在下丘脑的视交叉上核与视上核中，树鼩脑内检测到 ChAT-ir 神经元，但在小鼠脑内未发现。树鼩 ChAT-ir 神经元在尾状核、内侧隔核、脚桥核/背侧被盖核及前顶核中表现出更高的树突复杂度，而对角带水平支与动眼神经核在不同物种间则呈现相似的复杂度。在壳核区域，树鼩的远端树突比小鼠更为复杂，但近端分支的复杂度较低。ChAT-ir 神经元在尾状核中呈现头尾方向的密度梯度分布，而小鼠的 ChAT、CB、PV 及 CR 阳性神经元在尾状核壳核内侧与外侧区域分布基本均匀。这些发现全面绘制了树鼩脑内 ChAT-ir 神经元的分布图谱，突显了显著的种间差异，并为研究胆碱能神经元在多种神经功能中的作用提供了结构框架。

关键词：树鼩；胆碱乙酰转移酶；全脑图谱，壳核；尾状核

彭一林[1#]、王帅灯[1#]、汪懿[1]、张之仪[1]、张姗姗[1]、刘双双[1]、洪梓然[1]、徐琦琦[2]、杨跃雄[3]、刘芳[3]、母华伟[4]、王浩[4]、沈玥茹[2]、王宇[2]、秦新娅[2]、单庆红[2]、陈鹏[2]、刘荣玉[5]、周江宁[2]、汪琛玮[1,2*]

1 安徽医科大学基础医学院解剖学教研室，中国安徽省合肥市，230032。

2 安徽省合肥市安徽医科大学第一附属医院脑科学研究院，中国安徽省合肥市，230022。

3 昆明动物研究所，中国科学院，苏州大学-中国科学院昆明动物研究所疾病动物模型与新药研发联合实验室，学习记忆实验室，中国云南省昆明市，650223。

4 教育部脑启发智能感知与认知重点实验室、合肥国家微尺度物理科学研究中心、安徽生物医学成像与智能处理重点实验室、HFCNS 人工智能研究院、中国科学技术大学脑启发智能技术与应用国家工程实验室，中国安徽省合肥市，230026

5 安徽省合肥市安徽医科大学第一附属医院老年病研究所，中国安徽省合肥市 230022

#作者对本研究贡献均等

通讯作者：汪琛玮，cwwang@ahmu.edu.cn，86-551-65161047